# A mathematical model for the effects of amyloid beta on intracellular calcium

Joe Latulippe[1]*, Derek Lotito[2], Donovan Murby[1]

**1** Mathematics Department, Norwich University, Northfield, Vermont, United States of America, **2** Chemistry and Biochemistry Department, Norwich University, Northfield, Vermont, United States of America

* jlatulip@norwich.edu

## Abstract

The accumulation of Alzheimer's disease (AD) associated Amyloid beta (A$\beta$) oligomers can trigger aberrant intracellular calcium (Ca$^{2+}$) levels by disrupting the intrinsic Ca$^{2+}$ regulatory mechanism within cells. These disruptions can cause changes in homeostasis levels that can have detrimental effects on cell function and survival. Although studies have shown that A$\beta$ can interfere with various Ca$^{2+}$ fluxes, the complexity of these interactions remains elusive. We have constructed a mathematical model that simulates Ca$^{2+}$ patterns under the influence of A$\beta$. Our simulations shows that A$\beta$ can increase regions of mixed-mode oscillations leading to aberrant signals under various conditions. We investigate how A$\beta$ affects individual flux contributions through inositol triphosphate (IP$_3$) receptors, ryanodine receptors, and membrane pores. We demonstrate that controlling for the ryanodine receptor's maximal kinetic reaction rate may provide a biophysical way of managing aberrant Ca$^{2+}$ signals. The influence of a dynamic model for IP$_3$ production is also investigated under various conditions as well as the impact of changes in membrane potential. Our model is one of the first to investigate the effects of A$\beta$ on a variety of cellular mechanisms providing a base modeling scheme from which further studies can draw on to better understand Ca$^{2+}$ regulation in an AD environment.

## Introduction

Alzheimer's Disease (AD) is a devastating neurodegenerative illness affecting over 40 million people worldwide. AD is the leading cause of dementia and is characterized by a progressive and irreversible decline in memory and cognitive skills [1]. The prevalence of AD and associated dementia is estimated to double in the next 20 years, and as such, there is a critical need to better understand this disease. While the appearance of extracellular hydrophobic amyloid plaques and intracellular neurofibrillar tangles associated with tau proteins have become the hallmarks of the disease, the cause of AD remains unknown. Abnormal intracellular Ca$^{2+}$ levels have been observed in AD brains even before the presentation of clinical symptoms and amyloid plaques [2, 3]. Because it has been shown that Amyloid beta peptide (A$\beta$) accumulation can lead to increased intracellular Ca$^{2+}$ levels [4, 5], studying its effect on intracellular mechanisms is important for understanding its impact on neuronal functions. Intracellular

accumulation of Aβ can cause an increase release of $Ca^{2+}$ from internal stores such as the Endoplasmic Reticulum (ER) [4, 6–8]. As such, Aβ may lead to both local and global $Ca^{2+}$ proliferation that are persistent and cytotoxic. Sustained $Ca^{2+}$ disregulation can trigger apoptosis leading to premature neuronal death, a characteristic feature seen in AD. Although the accumulation of Aβ has been linked to the progression of AD by altering $Ca^{2+}$ signaling processes within neurons and neuroglia, the mechanisms for how and why this occurs are not fully understood.

Our goal is to use mathematical modeling to describe various conditions under which Aβ can lead to aberrant $Ca^{2+}$ signaling. The amyloid hypothesis suggests that the accumulation of Aβ in the brain is the primary driving force of AD pathogenesis [9–12]. In this hypothesis, the formation of Aβ plaques and fibrils are a consequence of the imbalance between the formation and sequestration of Aβ. The slow accumulation of Aβ peptides can alter $Ca^{2+}$ signaling processes leading to synaptic failure and neuronal death. Although it is unclear how Aβ disrupts intracellular $Ca^{2+}$ homeostasis, there is growing evidence that Aβ directly affects the production of inositol triphosphate ($IP_3$) [7], calcium-induced calcium release (CICR) through the ryanodine receptor (RyR) [13, 14], and the plasma membrane [15, 16]. We use the results of these works to make simplifying assumptions for how Aβ affects various $Ca^{2+}$ signaling mechanisms in a simplified whole-cell model.

In this study we present a theoretical approach to better understand the driving mechanisms for various $Ca^{2+}$ oscillatory patterns within an AD environment. By developing a mathematical model for intracellular $Ca^{2+}$ regulation, we can begin to study how Aβ affects $Ca^{2+}$ flux through various individual channels and pumps. Investigating model solutions can also provide important information on the impact of Aβ on $Ca^{2+}$ basal levels over various timescales. Due to current experimental limitations, mathematical and computational models can provide insights for targeting specific mechanisms in order to restore neuronal function, and to suggest symptomatic improvement strategies. In fact, according to Liang et al. (2015) there is growing momentum to study $Ca^{2+}$ dynamics in AD, specifically through computational and mathematical modeling, and this work outlines such an approach.

## Methods

### Calcium model formulation

In order to study the effects of Aβ on intracellular $Ca^{2+}$, we first build a simplified whole-cell $Ca^{2+}$ model by making use of the vast array of work on modeling $Ca^{2+}$ dynamics and the calcium signaling "toolkit" (see [17–20] for example). Once this model is developed, we add the influence of Aβ by altering various components of the model. We then analyze model solutions by investigating the dynamical structure for various parameter regimes in order to draw out conditions that lead to changes in basal $Ca^{2+}$ levels and aberrant signals. For our purposes, we characterize aberrant signals as non-periodic oscillations over a timescale of about 100-200 seconds.

We model $Ca^{2+}$ dynamics using traditional methods by tracking the flux in and out of the cytoplasm. Let $c$ denote the concentration of free $Ca^{2+}$ ions in the cell cytoplasm, then the rate of change in intracellular $Ca^{2+}$ is governed by

$$\frac{dc}{dt} = \tilde{J}_{in} - \tilde{J}_{out},$$  (1)

where $\tilde{J}$ denotes flux. We assume a spatially homogeneous cell whose volume is fixed and track $Ca^{2+}$ concentration changes in time. As such, the ER and cytoplasm coexist at each point of the cell. Although these simplifying assumptions make the model limited, such an approach

has been extremely useful in quantifying and identifying key mechanisms behind certain $Ca^{2+}$ signaling patterns. We take this position to study the influence of $A\beta$ on $Ca^{2+}$ dynamics using a simplified whole-cell model. Many different mathematical approaches have been used to better understand $Ca^{2+}$-mediated neuroglia function (see [21] for an overview of these) and we have utilized this body of work to develop our model below.

Our model structure was selected to account for the major components that have been shown to be influenced by $A\beta$ and that can lead to $Ca^{2+}$ dynamics on the timescale of seconds. We assume that intracellular $Ca^{2+}$ in-fluxes (into the cytoplasm) are those corresponding to IP$_3$ receptors (IPR), RyRs, a general membrane leak $J_{in}$, and we include a fast Voltage Gated $Ca^{2+}$ Channel (VGCC) in $J_{vca}$ to account for membrane permeability. The out-fluxes (out of the cell or sequestered into $Ca^{2+}$ pools such as the ER) are modeled using a plasma membrane pump $J_{pm}$, and a sarco-endoplasmic reticulum $Ca^{2+}$ ATPase (SERCA) pump $J_{SERCA}$. A diagram of the major fluxes outlined in the model is given in Fig 1. Also included in the diagram are the model assumptions of the interaction of $A\beta$ with respect to individual flux term.

We assume that the ER is homogeneously distributed throughout the interior of the cell and that the fluxes of $Ca^{2+}$ through the IPR and RyR are proportional to the difference in the concentration of $Ca^{2+}$ between the ER and the cytoplasm. Under these standard assumptions,
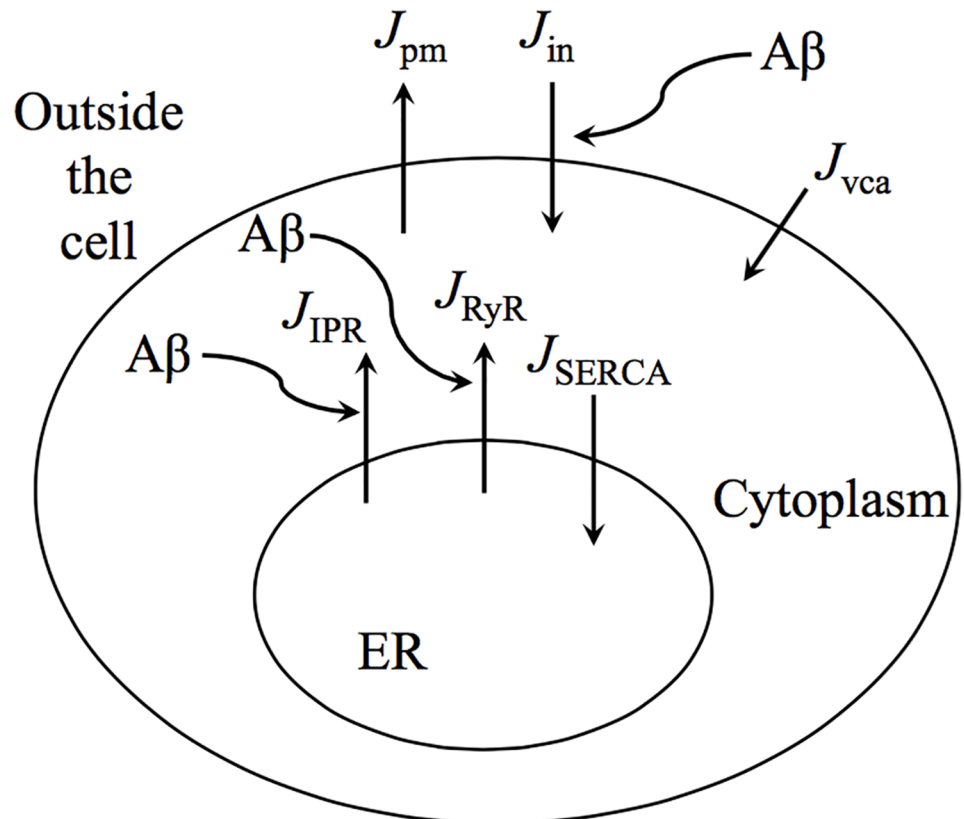


**Fig 1. Two pool model diagram.** This figure shows the critical flux terms utilized in the formulation of the model. In addition, the relevant fluxes affected by $A\beta$ are highlighted.

using conservation of fluxes, our general $Ca^{2+}$ model takes the form

$$\frac{dc}{dt} = J_{IPR} + J_{RyR} - J_{SERCA} + J_{in} - J_{pm} + J_{vca} \tag{2}$$

$$\frac{dc_e}{dt} = -\gamma(J_{IPR} + J_{RyR} - J_{SERCA}) \tag{3}$$

where $c_e$ denote the concentration of $Ca^{2+}$ in the ER, and $\gamma$ is the ratio of cytoplasmic volume to the ER volume. The individual contributions of each flux can vary from a simple Hill function to more complicated forms involving numerous parameters and additional terms. We provide a description of each of the flux terms we use in our model below. We also provide background information on their development and why it may be well suited for our purposes. Each term was chosen in order to balance meaningful biophysical quantities while maintaining a tractable mathematical structure.

The term $J_{vca}$ in (2) links membrane potentials with other $Ca^{2+}$ signaling mechanisms. $Ca^{2+}$ regulation and changes in membrane potential do depend on each other and a model that connects their influence may be critical for advancing our understanding of the long term effects of A$\beta$ on $Ca^{2+}$ signaling. To address this, we include a section in our results that incorporates the effects of membrane potentials into our model and provide some examples of the impact of A$\beta$ on the dynamics. Although a full exploration of the role of membrane potential on $Ca^{2+}$ dynamics is beyond the scope of the current study, we do provide the base structure from which to build a more complete whole-cell model.

$Ca^{2+}$ regulation in non-excitable cells, such as astrocytes, is extremely complex and influenced not only by membrane potential but also $Ca^{2+}$ buffering. Cytoplasmic $Ca^{2+}$ buffering plays a significant role in calcium's ability to move throughout the cell. Almost all of the available $Ca^{2+}$ is bound to buffers and free cytoplasmic $Ca^{2+}$ cannot move very far before being bound [18]). Because $Ca^{2+}$ diffusion plays an important role in spatiotemporal signaling, non-linear buffering may provide some insights behind certain types of oscillatory patterns and $Ca^{2+}$ waves. However, compared to the temporal release and uptake of $Ca^{2+}$ into internal stores, buffering occurs on a much faster timescale. In our model we have assumed that $Ca^{2+}$ buffering is fast, immobile, and has low affinity. Using these assumptions, we have scaled the model to account for fast and linear buffers even though an explicit description of buffering is not provided (further details on buffering can be found in [18]).

**IP$_3$ receptor model.** IP$_3$ is a ligand produced by phospholipase C (PLC) when activated by a G-protein coupled receptor reacting to an external stimulus such as neurotransmitters, hormones, and growth factors [22]. As a key secondary messenger, IP$_3$ regulates many important cellular functions, including the release of $Ca^{2+}$ from the ER through the IP$_3$ receptor [23]. We assume that the flux from the IP$_3$ receptor follows a saturating binding rate model of the form found in [24, 25]. Thus, we write

$$J_{IPR} = (k_f P_0 + J_{er})(c_e - c) \tag{4}$$

where $k_f$ controls the density of the IP$_3$ receptor, $J_{er}$ is a leak from the ER to the cytoplasm, and $P_0$ is the open probability of the IPR. The leak term is necessary to balance the ATPase flux at steady state. To model $P_0$, we use a version of the Sneyd and Dufour (2002) model that is based on previous models found in [26–28]. The model assumes that the receptor can be in one of six states, with $R$ the resting state, $O$ the open state, $A$ the active state, $S$ the shut state, and $I_1$ and $I_2$ both represent inactive states. The transitions between states can depend on $Ca^{2+}$ and IP$_3$ concentration $p$. As such, the IP$_3$ receptor will be in various states depending on the value of $p$.

In this model, the receptor open probability is given by

$$P_0 = (\alpha_1 O + \alpha_2 A)^4 \tag{5}$$

where $\alpha_1$ and $\alpha_2$ are parameters that control the individual contributions of the open and active states of the receptor. As in [24], we assume that $\alpha_1 = 0.1$ and $\alpha_2 = 0.9$. In the model, it is assumed that the receptor has four identical and independent subunits and that $Ca^{2+}$ flows when all four subunits are in either the $O$ or $A$ state. The equations for the transitions between the states are given in [24], but have also been included in the Supplementary Appendix for completeness. This model was chosen since it does respond reasonably well to changes in $Ca^{2+}$ concentration and $IP_3$ concentrations [25].

**RyR model.** To model the contribution of the RyR, we utilize the algebraic model of Friel (1995). The receptor is modeled as a simple leak channel, with a flux through the channel proportional to the concentration difference between the ER and cytosol. This model was used to investigate $Ca^{2+}$ oscillations in a sympathetic neuron. Thus, the flux through the RyR is given by

$$J_{RyR} = k_3(c_e - c). \tag{6}$$

To more accurately model CICR, the rate constant $k_3$ is defined as an increasing sigmoidal function of intracellular $Ca^{2+}$ concentration and takes the form

$$k_3 = k_1 + \frac{k_2 c^n}{k_d^n + c^n}, \tag{7}$$

where $k_1$, $k_2$, and $k_d$ are parameters. We use $n = 3$ to match the experimental results obtained in [29]. The parameter $k_1$ in (7) is the zero calcium concentration level leak. This term is often used to ensure a physiologically significant resting $Ca^{2+}$ level [18]. The term $k_d$ corresponds to the RyR channel sensitivity for CICR, and $k_2$ is the maximal rate of the channel. The simple nature of the Friel model makes it a viable choice especially since data for the contributions of $Ca^{2+}$ flux through the RyR in the presence of $A\beta$ are minimal.

**Leak, membrane pump, and SERCA.** The membrane leak $J_{in}$ is modeled using a linearly increasing function of $IP_3$ concentration [30]. Although this increase may be due to various mechanisms, here we only include a linearly increasing contribution to make sure that steady-state $Ca^{2+}$ concentration depend on $p$. Thus,

$$J_{in} = a_1 + a_2 p, \tag{8}$$

where $a_1$ and $a_2$ are parameters.

When modeling $Ca^{2+}$ dynamics both the SERCA pump and the plasma membrane pump play an important role in maintaining concentration gradients. Different models of these pumps exist and vary in complexity. Here we model the plasma membrane pump using a simple Hill equation of the form

$$J_{pm} = \frac{V_{pm} c^n}{K_{pm}^n + c^n}, \tag{9}$$

where $V_{pm}$ is the maximal velocity and $K_{pm}$ is the channel sensitivity. We have chosen a standard Hill coefficient of 2 as is found in [31].

To describe the behavior of the SERCA pump we utilize a simplified four state bidirectional Markov model (as found in [20]) of the form

$$J_{serca} = \frac{c - K_1 c_e}{K_2 + K_3 c + K_4 c_e + K_5 c c_e}$$ (10)

to model the SERCA pump. In (10), $K_i$ for $i = 1, \ldots, 5$ are constants. Notice that this choice of model is more complicated than a simple Hill equation. Experimental evidence show that the rate of the pump may be modulated by the level of $Ca^{2+}$ in the ER [32, 33], and this model provides a way to account for both $c$ and $c_e$.

**Voltage dependent calcium channel.** The flux due to changes in membrane potential is given in our model by $J_{vca}$. When the volume of the cell is constant, $Ca^{2+}$ flux and current are related by the equation

$$J_{vca} = \frac{-I_{ca}}{2Fw},$$ (11)

where $I_{ca}$ is the current through the VGCC, $F$ is Faraday's constant, and $w$ is the cell volume. Since $I_{ca}$ depends on the membrane potential $V$ and $Ca^{2+}$, we need a way to track membrane potential. Here, we assume that the membrane potential follows a Hodgkin and Huxley formulation [34] that satisfies

$$C_m \frac{dV}{dt} = -\sum I_x,$$ (12)

where $C_m$ is the cell capacitance, $V$ is the membrane potential, and the sum is over all ionic currents across the cell membrane. In the case of non-excitable astrocytes, current flow across its membrane is characterized by potassium ($K^+$)-selective membrane conductance [35] and voltage dependent channels [36, 37]. As such, our membrane equation takes the form

$$C_m \frac{dV}{dt} = -I_{kir}(V) - I_{na}(V) - I_l(V) - I_{ca}(V) + I_{app},$$ (13)

where $I_{kir}$, $I_{na}$, $I_l$, and $I_{ca}$ correspond to an inward rectifying potassium, sodium, leak, and $Ca^{2+}$ current, respectively, and $I_{app}$ is an applied current. In (13), we utilize a formulation for $I_{kir}(V)$ similar to [38] and write

$$I_{kir}(V) = -g_{kir}\left(\frac{\sqrt{K_0}}{1 + \exp((V - V_{ka} - V_{a2})/V_{a3})}\right)(V - V_{ka} - V_{a1}),$$ (14)

where $g_{kir}$ is the maximal channel conductivity, $V_{ka}$ is the Nernst $K^+$ potential, $K_0$ is the extracellular $K^+$ concentration, and $V_{a1}$, $V_{a2}$ and $V_{a3}$ are constants. In the model of [38], $K_0$ is time dependent and depends on proximal neuronal activity (further details of this formulation can be found in [38]). Here, we simplify this and assume that the external compartment is saturated with $K^+$ and as such consider $K_0$ to be constant. Each of the remaining currents have the form $I_x = g_x(V - V_x)$, where $g_x$ is the conductance and $V_x$ is the Nernst potential of each channel.

Although many alternative formulations for $I_{ca}$ exist (such as the Goldman-Hodgkin-Katz current approximation), we use a T-type like channel (as that found in [39]) of the form

$$I_{ca}(V) = \bar{g}_{caT} m_{caT}^2 h_{caT}(V - V_{ca}),$$ (15)

where $\bar{g}_{caT}$ is the maximal conductance, $V_{ca}$ is the $Ca^{2+}$ Nernst potential, and $m_{caT}$ and $h_{caT}$ are gating variables similar to those used for the $Na^+$ channel in the Hodgkin and Huxley model.

A T-type $Ca^{2+}$ current has a low-threshold activation with an inactivating gating variable that exhibit sub-threshold oscillations and inhibitory rebound bursts. Although other types of $Ca^{2+}$ currents (such as L-type, $Ca^{2+}$-dependent potassium channels, etc.) can also be included in the model, here we simply illustrate how one can link membrane potential with other $Ca^{2+}$ regulatory mechanisms together into a single model and use that model to investigate the role of $A\beta$ on $Ca^{2+}$ dynamics. As such, the T-type $Ca^{2+}$ channel described in (15) is sufficient for studying how changes in membrane potentials could impact intracellular $Ca^{2+}$. Full details of the membrane potential model are provided in the Supplementary Appendix.

### Amyloid beta assumptions

The influence of $A\beta$ on individual pumps, channels, and exchangers remains largely unknown. However, some studies provide insight on the effects of $A\beta$ on $Ca^{2+}$ regulation and we utilize these findings in making our assumptions about the effects of $A\beta$. For example, De Caluwé and Dupont (2013) formalized a theoretical model to describe a possible feedback loop between $Ca^{2+}$ and $A\beta$. Their model showed that the existence of a bistable steady-state region can exists in the presence $A\beta$. The model suggests that over time, cytosolic $Ca^{2+}$ proliferation as a result of $A\beta$ could trigger the onset of AD. In this study, we are interested in the generation of aberrant $Ca^{2+}$ signals on a relatively short timescale. Since the accumulation of $A\beta$ can occur over months, years, and even decades, $A\beta$ concentrations changes occur on a very long timescale compared to changes in $Ca^{2+}$. As such, we assume that $A\beta$ may be present in the environment, but make no attempt to track changes in $A\beta$ concentration over time.

The formation of $A\beta$ plasma membrane pores can alter $Ca^{2+}$ signaling by creating additional influx into the cytoplasm [15, 16, 40, 41]. In order to incorporate the possible influence of $A\beta$ generated plasma membrane pores, we use a similar mechanism as found in [42]. Let $a$ represent a fixed level of $A\beta$ concentration present in the environment. Then, we include the term $k_\beta a^m$ in $J_{in}$ and write an altered membrane leak flux as

$$J_{in} = a_1 + a_2 p + k_\beta a^m, \tag{16}$$

where $m$ represents a cooperativity coefficient, and $k_\beta$ is a rate constant (see [42] for details).

Although it is well known that $A\beta$ can disrupt RyR-regulated $Ca^{2+}$ signals, the mechanisms for how this happens remains controversial [43–45]. Several studies have addressed the role of RyR-regulated $Ca^{2+}$ disruptions in AD [46–49]. Paula Lima et al. (2011) report that $A\beta$ can generate prolonged $Ca^{2+}$ signals *in vitro* through RyR in primary hippocampal neurons of rat embryos as a result of NMDAR-dependent $Ca^{2+}$ entry through the plasma membrane. These results agree with studies showing that $A\beta$ can cause substantial $Ca^{2+}$ influx through NMDAR [50, 51]. In our model these types of fluxes are combined and accounted for in $J_{in}$, although in a somewhat crude fashion. Futhermore, $A\beta$ can increase RyR channel open probability on a short timescale [4, 14]. In order to account for this, we alter the RyR channel sensitivity term and assume that it is affected by $A\beta$. Thus, our altered RyR model takes the form

$$k_3 = k_1 + \frac{k_2 c^n}{(k_d + k_\alpha a)^n + c^n}, \tag{17}$$

where $k_\alpha$ is positive and controls the strength of the influence of $A\beta$. Notice that an increase in $a$ corresponds to an increase in the RyR sensitivity.

**Calcium model formulation with amyloid beta.** The simplified whole-cell $Ca^{2+}$ model described above tracks changes in cytosolic $Ca^{2+}$ concentration as a function of time in the presence of $A\beta$. By putting the different channels, exchangers, and pumps together, our $Ca^{2+}$

model takes the form

$$
\begin{aligned}
\frac{dc}{dt} &= \left( k_f (0.1O + 0.9A)^4 + k_1 + \frac{k_2 c^3}{(k_d + k_\alpha a)^3 + c^3} \right)(c_e - c) \\
&\quad - \frac{c - K_1 c_e}{K_2 + K_3 c + K_4 c_e + K_5 c c_e} + (a_1 + a_2 p + k_\beta a^m) - \frac{V_{pm} c^2}{K_{pm}^2 + c^2} \\
&\quad - p_s \bar{g}_{caT} m_{caT}^2 h_{caT} (V - V_{ca}),
\end{aligned}
\tag{18}
$$

$$
\begin{aligned}
\frac{dc_e}{dt} &= -\gamma \left[ \left( k_f (0.1O + 0.9A)^4 + k_1 + \frac{k_2 c^3}{(k_d + k_\alpha a)^3 + c^3} \right)(c_e - c) \right. \\
&\quad \left. - \frac{c - K_1 c_e}{K_2 + K_3 c + K_4 c_e + K_5 c c_e} \right].
\end{aligned}
\tag{19}
$$

Notice that this model has twelve dynamic equations, with five of those controlling the IP$_3$ receptor ($R$, $O$, $A$, $I_1$, and $I_2$), three controlling the membrane potential ($V$, $m$, and $h$), and an additional two variables controlling the gating variables $m_{caT}$ and $h_{caT}$ (a description of these additional equations are provided in the Supplementary Appendix). We have also added a scaling and control parameter $p_s$ to simplify the contribution from the VGCC flux. When $p_s = 0$, the impact of membrane potential on Ca$^{2+}$ signaling are ignored. When $p_s > 0$, changes in membrane potential do influence the dynamics of intracellular Ca$^{2+}$. The large set of parameter values was selected to closely match those of previous studies whenever possible and can be found in Table 1.

In the formulation of our model we have assumed that the presence of A$\beta$ can increase membrane permeability by creating plasma membrane A$\beta$ pores, and have used the work of

**Table 1. Parameter values of the Ca$^{2+}$ model (18) and (19).**

| Parameters | | | |
|---|---|---|---|
| $k_f$ | 0.98 s$^{-1}$ | $\gamma$ | 5.4 |
| RyR | | | |
| $k_1$ | 0.013 s$^{-1}$ | $k_d$ | 0.13 $\mu$M |
| $k_2$ | 0.18 s$^{-1}$ | $k_\alpha$ | .75 |
| SERCA | | | |
| $K_1$ | 0.0001 | $K_2$ | 0.007 s |
| $K_3$ | 0.06 $\mu$M$^{-1}$ s | $K_4$ | 0.0014 $\mu$M$^{-1}$ s |
| $K_5$ | 0.007 $\mu$M$^{-2}$ s | | |
| Transport | | | |
| $a_1$ | 0.003 $\mu$M s$^{-1}$ | $k_\beta$ | 1 s$^{-1}$ |
| $a_2$ | 0.02 s$^{-1}$ | $m$ | 4 |
| $V_{pm}$ | 2.8 $\mu$M s$^{-1}$ | $K_{pm}$ | 0.425 $\mu$M |
| K$^+$ Channel | | | |
| $g_{kir}$ | 60 pS | $K_0$ | 2 mM |
| $V_{a1}$ | -14.83 mV | $V_{a2}$ | 34 mV |
| $V_{a3}$ | 19.23 mV | $V_{ka}$ | -65.2 mV |
| VGCC | | | |
| $\bar{g}_{caT}$ | .45 mS $\cdot$ ms$^{-1}$ | $V_{ca}$ | 100 mV |

[42] to alter our membrane in-flux. Additionally, we have assumed that the presence of A$\beta$ increases RyR sensitivity and have incorporated additional terms in the RyR component of the model. Currently in our model, IP$_3$ acts as the primary agonist that can then trigger Ca$^{2+}$ release from IP$_3$ receptors. In addition to affecting the IP$_3$ receptor open probability, Ca$^{2+}$ release activates RyR and subsequent CICR. In the next chapter we separate our analysis for the model under three assumptions. We first characterize the solutions of the model for constant levels of IP$_3$ and when the effects of membrane potential are ignored. Second, also in the absence of membrane potentials, we expand our model to include a dynamic variable for IP$_3$ production. Lastly, we include the effects of membrane potential on Ca$^{2+}$ dynamics by incorporating flux through VGCC under various levels of fixed IP$_3$. We further look to characterize the impact of VGCC on model solutions in the presence of A$\beta$.

Numerical solutions of the differential equations systems were obtained using explicit Runge-Kutta (4,5) algorithms implemented in Matlab [52]. Bifurcation analyses were done using the AUTO [53] extension of XPPAUT [54]. AUTO is a software program used to analyze the bifurcation structures of systems of ordinary differential equations such as (18) and (19). In the bifurcation diagram illustrated in this manuscript, the bifurcation parameter is plotted on the $x$-axis and the projection of stable and unstable steady-state solutions, upper and lower branches of periodic orbits, and critical transitions points (such as Hopf and period doubling) are labeled accordingly. Hopf bifurcations occur when a steady-state solution loses it's stability as a result of small changes in a parameter. Mathematically, this occurs when complex eigenvalues (of the linearization) cross the imaginary axis away from the origin. Period doubling bifurcations occur when a small change in a bifurcation parameter causes the period of an oscillatory system to double. These and other types of bifurcations can be used to describe systemic changes in dynamics and in our case, transitions from single-mode oscillations to mixed-mode oscillations (MMOs). The program AUTO allows us to readily compute the location of these bifurcations as model parameters are varied. Initial conditions for all simulations were set at $c_0 = 0.05$ and $c_e = 10$ with $R_0 = 1$ and all other IP$_3$ receptor initial conditions are set to zero. Initial conditions for the membrane potential are $V_0 = -65$, $m_0 = 0.05$, $n_0 = 0.32$, $h_0 = 0.6$, $m_{caT0} = 0.29$, and $h_{caT0} = 0.01$.

## Results

In all three sections below, the model dynamics show that aberrant Ca$^{2+}$ can emerge in the presence of A$\beta$. These aberrant signals can occur under various conditions suggesting a complex link between the influence of A$\beta$ and the model components. As such, we break down the dynamics of the model by tracking solutions as a result of altering one or two parameters within a specific signaling component. We first look at model solutions when IP$_3$ concentration is fixed and persists and is not influenced by membrane potential. We then allow for IP$_3$ to change dynamically and simulate the response in Ca$^{2+}$ with and without the influence of A$\beta$. Lastly, we incorporate the influence of membrane potentials and investigate model solutions for various levels of A$\beta$ when IP$_3$ concentration is fixed.

### Calcium model with constant IP$_3$ and no membrane potential

Simulations of (18) and (19) with $p_s = 0$ show that incorporating A$\beta$ in a simplified Ca$^{2+}$ model can lead to aberrant Ca$^{2+}$ signaling through dynamical transitions into MMOs. Particularly, we look to track the influence of A$\beta$ on the location of Hopf points (labeled HB), period doubling points (labeled PD), and regions of MMOs (shaded) in order to better understand Ca$^{2+}$ steady-states and oscillatory patterns. From a phenomenological perspective, a transition through MMO may explain why A$\beta$ can trigger persistent aberrant Ca$^{2+}$ signals. Although the

long-term accumulation and influence of A$\beta$ remains difficult to model, our approach illustrates that aberrant Ca$^{2+}$ signals can occur under the influence of A$\beta$ for a variety of parameter regimes.

**IP$_3$ influence on model dynamics.** Experimentally, IP$_3$ can be photoreleased simultaneously through out a cell. In such conditions, IP$_3$ diffusion is minimized and can be treated as constant. By varying the amount of IP$_3$ available in the cytosol, the model can exhibit Ca$^{2+}$ oscillations as typically found in various cell types. These oscillatory patterns are critical in order for cells to maintain appropriate concentration gradients and to re-establish homeostasis levels after a triggering event. In the absence of A$\beta$, model Ca$^{2+}$ oscillations appear and disappear as a result of transitions through Hopf bifurcations as the parameter $p$ increases. Although these stable oscillatory patterns are predictable for a large domain of the parameter $p$, the model does exhibit MMOs for small parameter regions near the Hopf points. It is these MMO patterns that we are most interested in. Our results show that in the presence of A$\beta$, the regions of MMOs can grow and become larger. This leads to an increased possibility for aberrant Ca$^{2+}$ signals. We hypothesize that aberrant Ca$^{2+}$ signals observed experimentally can be described as dynamic transitions through MMOs. The complicated patterns in MMOs are often characterized by sub-threshold oscillations interspersed within large relaxation types of oscillations [55–57].

Illustrated in Fig 2A and 2B are numerical simulations of the model, with $a = 0$ that exhibit sustained Ca$^{2+}$ oscillations as the amount of $p$ is increased from $p = 5$ to $p = 10$. An increase in frequency occurs as $p$ increases within the predictable region and can be seen by comparing Fig 2A and 2B. In Fig 2C, a partial bifurcation diagram showing the stable maximum and minimum periodic amplitudes is given along with the regions of MMOs and the critical transitions points. Fig 2D shows the solution of the model for $p = 18.5$. For this $p$-value, the model undergoes MMOs with varying oscillatory patterns of mixed amplitude, but we do not characterize it as aberrant Ca$^{2+}$ signaling since it is periodic. Notice that no Ca$^{2+}$ oscillations occur for small and large values of $p$. This is due to the assumption that the IP$_3$ receptor is unlikely to open at high and low concentrations of IP$_3$. Although our model does not exhibit a typical Hopf bubble, it has the overall qualitative patterns of a robust Ca$^{2+}$ model as described in [18].

**The presence of amyloid beta.** We consider an AD environment where some accumulation of A$\beta$ has occurred but assume that this amount is fixed during the timescale of our simulations. As such, we assume that $a$ is constant and that the value correlates to the concentration of A$\beta$ in $\mu$M. That is, the value of $a$ in the model may be thought of as reflecting the stage of the progression of the disease. For example, a small value of $a$ corresponds to a small amount of A$\beta$ that may have accumulated in the early stages of AD, while a larger value of $a$ may correspond to a late stage AD. As the parameter $a$ is varied, we can then study how the dynamics of the model change as the level of A$\beta$ changes. Our ultimate goal is to better understand the implications of various levels of A$\beta$ on Ca$^{2+}$ so that we may gain knowledge about the possible progression of AD.

**The effects of A$\beta$ on calcium steady-state levels.** The accumulation of A$\beta$ can lead to increased steady-state levels as well as large amplitude oscillations even in the absence of IP$_3$ signaling. To better understand the effects of A$\beta$ on model solutions, we simulate the model and look at the effects of changing the parameter $a$ on steady-state levels. Various experimental studies have used A$\beta$ levels of 0.5 and 1.0 [13, 50, 51]. As such, we consider a range of values for $a$ that matches these types of levels.

In the case when no IP$_3$ is present, the accumulation of A$\beta$ increases the steady-state of Ca$^{2+}$ and can even lead to large-amplitude Ca$^{2+}$ oscillations. Illustrated in Fig 3A is a bifurcation diagram generated by changing the parameter $a$ when $p = 0$. Notice that the steady-state value slowly increases as $a$ increases until solutions transition into stable periodic oscillations
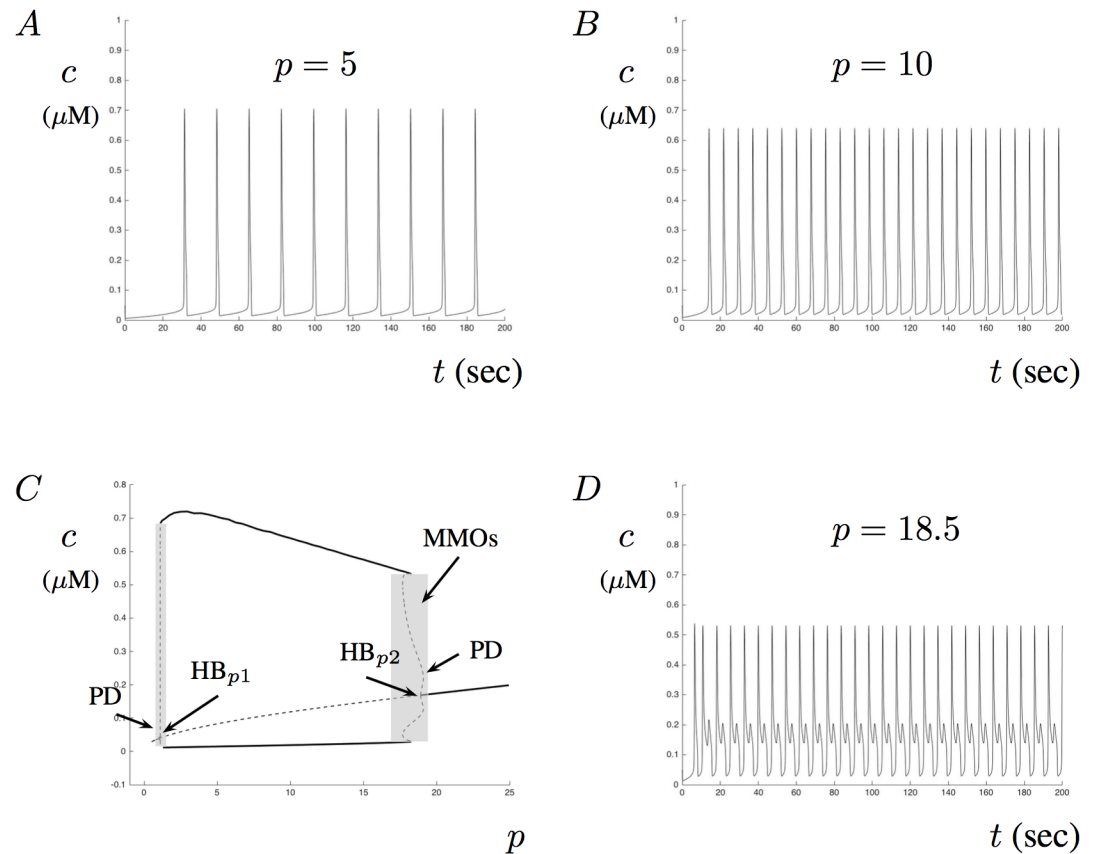
Fig 2. Calcium dynamics for constant IP$_3$ levels. Properties of the Ca$^{2+}$ model when IP$_3$ concentrations are fixed and no A$\beta$ is present (i.e., $a = 0$). A and B show the numerical solution with $p = 5$ and $p = 10$, respectively. For these parameter values, the frequency of oscillations increases as $p$ increases. C illustrates the partial bifurcation diagram for the model with $p$ as the bifurcation parameter. The middle curve crossing the diagram correspond to the steady-state values (solid for stable, dashed for unstable). Also shown are the maximum and minimum amplitudes of the periodic orbits of the model (solid curves above and below the steady-state curve). Key bifurcation points are labeled HB$_{p1}$ and HB$_{p2}$ (Hopf), and PD (period-doubling). The shaded area corresponds to the regions where MMOs are present. D shows MMOs for $p = 18.5$.

between the two Hopf points HB$_{a1}$ and HB$_{a2}$. As $a$ increases towards the value of 1.293, the steady-state asymptotes and solutions quickly become non-physical. Fig 3B shows a solution where large amplitude oscillations exist for $a = 1.15$. Fig 3C shows the solution for $a = 1.276$. Notice that in this case, the solution first undergoes a large Ca$^{2+}$ increase before settling in on a steady-state value. When the model is presented with levels of A$\beta$ greater than $a = 1.29$, solutions become intractable and are not analyzed.

**Two Parameter Analysis.** Since both $a$ and $p$ can affect the dynamics of the model, we look at their effects together. Given in Fig 4A is a partial two-parameter bifurcation set for the whole-cell model (18) and (19) when $p_s = 0$ using $p$ and $a$ as the bifurcation parameters. The solid lines correspond to the Hopf bifurcation manifolds, while the dashed lines correspond to the period-doubling manifolds. The shaded area in Fig 4A corresponds to the parameter values that elicit MMOs. Notice that in addition to the large MMO region between the dashed lines, there is a small thin region near the Hopf bifurcation manifold labeled HB$_2$ $m$. These MMOs vanish for values of $a > 0.275$. This bifurcation diagram has a number of interesting features that can bring to light important behavior in Ca$^{2+}$ regulation. For example, when $0.415 < a < 0.472$ the bifurcation diagram has four Hopf points. This leads to small amplitude
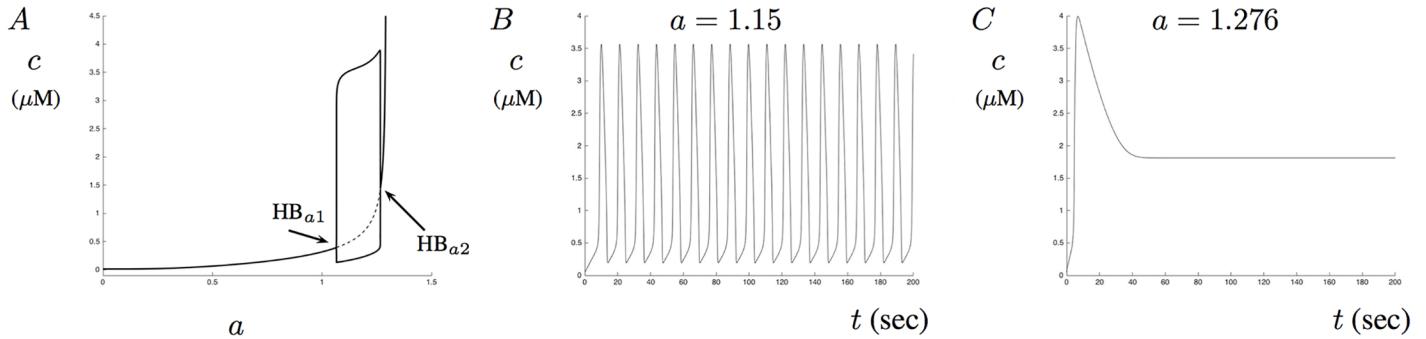
**Fig 3. The effects of Aβ on steady-state levels.** This figure shows the effects of Aβ on the steady-state $Ca^{2+}$ levels in the absence of $IP_3$. A shows a bifurcation diagram with $a$ as the bifurcation parameter. Two Hopf bifurcations, labeled $HB_{a1}$ and $HB_{a2}$, give rise to a Hopf bubble with relatively large oscillation amplitude. The steady-state level quickly becomes unphysical as the amount of Aβ increases towards $a = 1.3$. B shows stable $Ca^{2+}$ oscillations for $a = 1.15$. C shows the solution when $a = 1.276$.

oscillations for certain ranges in the parameter $p$. Fig 4B shows the bifurcation diagram when $a = 0.45$. In this diagram, three of the Hopf bifurcations have been labeled as $HB_1$ since all three points lie on the Hopf manifold labeled $HB_1m$ in Fig 4A.

To help us understand this bifurcation structure, various solutions are plotted in Fig 5 and compared to the bifurcation structure given in Fig 4. In Fig 5, $a = 0.45$ is kept fixed while various values of $p$ are used. The corresponding model solutions show different types of behaviors ranging from steady-state $Ca^{2+}$ levels, stable periodic solutions, aberrant $Ca^{2+}$ signals, and MMOs. Illustrated in Fig 5A is solution that exhibits small amplitude oscillations with $p = 5$. This solution corresponds to the region where the small Hopf bubble exists as shown in Fig 4B. Fig 5B shows a solution that reaches a stable steady-state when $p = 20$. Fig 5C and 5D show two different solutions that exhibit MMOs for $p = 26$ and $p = 45.5$, respectively. Fig 5D shows aberrant $Ca^{2+}$ signals when $p = 45.8$. Notice that this solution enters aberrant oscillations as the bifurcation structure transitions through period doubling points within the MMO region. Fig 5D shows sustained $Ca^{2+}$ oscillations when $p = 50$.
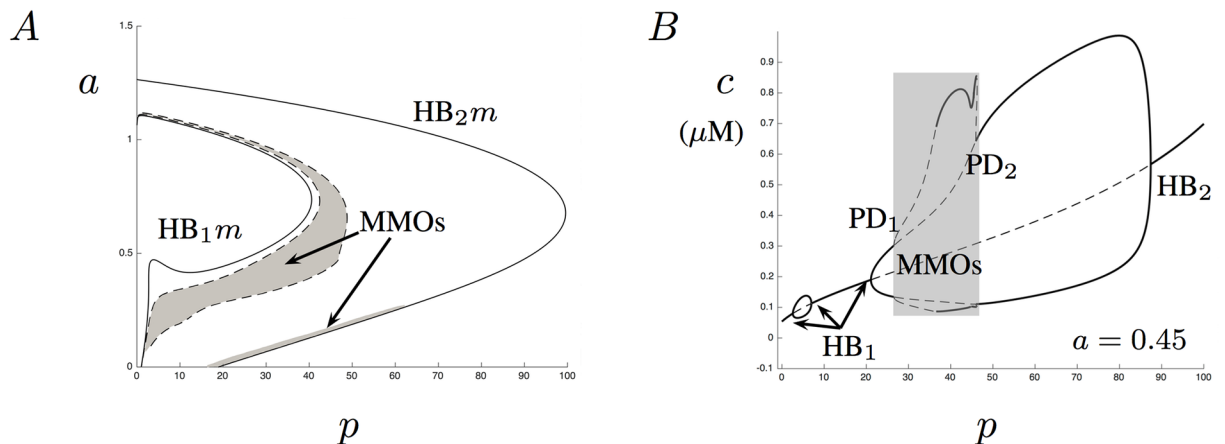


**Fig 4. Two parameter bifurcation.** A shows a two parameter bifurcation diagram when $p$ and $a$ are varied. The solid curves in the diagram correspond to the Hopf bifurcation manifolds and are labeled $HB_{1m}$ and $HB_{2m}$. The dashed lines correspond to manifolds of period doubling points. The shaded regions (between the dashed lines and near the bottom of $HB_2 m$) correspond to regions where MMOs occur. B shows a bifurcation diagram for $a = 0.45$. Notice that for this value of $a$, four Hopf bifurcations exist and three of them have been labeled with $HB_1$ while the last is labeled $HB_2$. This figure also illustrates the intermediate region of MMOs between the labels $PD_1$ and $PD_2$.
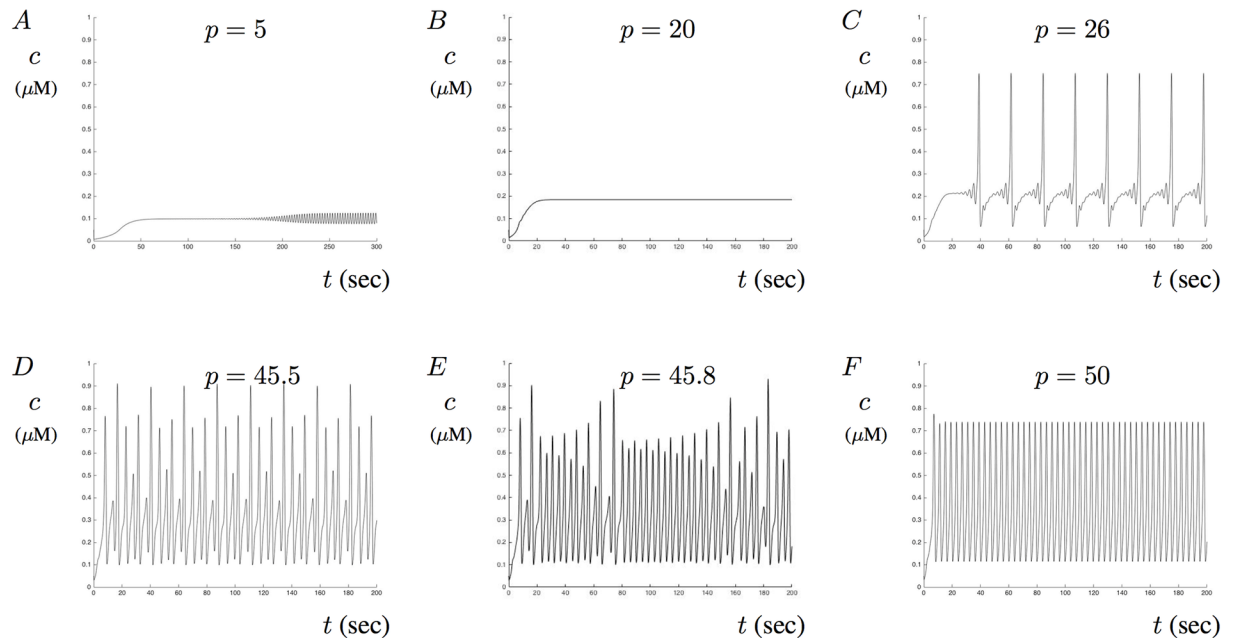
**Fig 5. Calcium oscillations in the presence of A$\beta$.** This figure shows various solutions when $a = 0.45$. A shows small amplitude oscillations when $p = 5$ while B shows a stable-steady state solution when $p = 20$. C and D both show MMOs with multiple sub-threshold oscillations when $p = 26$ and $p = 45.5$, respectively. E shows aberrant Ca$^{2+}$ signals when $p = 45.8$. F shows sustained Ca$^{2+}$ oscillations when $p = 50$.

https://doi.org/10.1371/journal.pone.0202503.g005

The results of the two parameter bifurcation analysis seem to suggest that A$\beta$ not only increases the steady-state level, but also influences the regions of MMOs. Particularly, the internal range where MMOs emerge between the Hopf manifolds increases for a large parameter range of $a$. As such, the model suggests that A$\beta$ may drive aberrant Ca$^{2+}$ signals as transitions through MMOs. However, as the simulated amount of A$\beta$ increases towards $a = 1$, the region of MMOs decreases and stable periodic orbits exist for most of the $p$ parameter range. This condition is illustrated in Fig 6 where two solutions are shown for relatively large values of $a$. Fig 6A shows the solution for $a = 1$ with $p = 30$, while B shows the solution for $a = 1.2$ and $p = 20$. In these cases, Ca$^{2+}$ oscillations have much larger amplitudes than in the absence of A$\beta$.
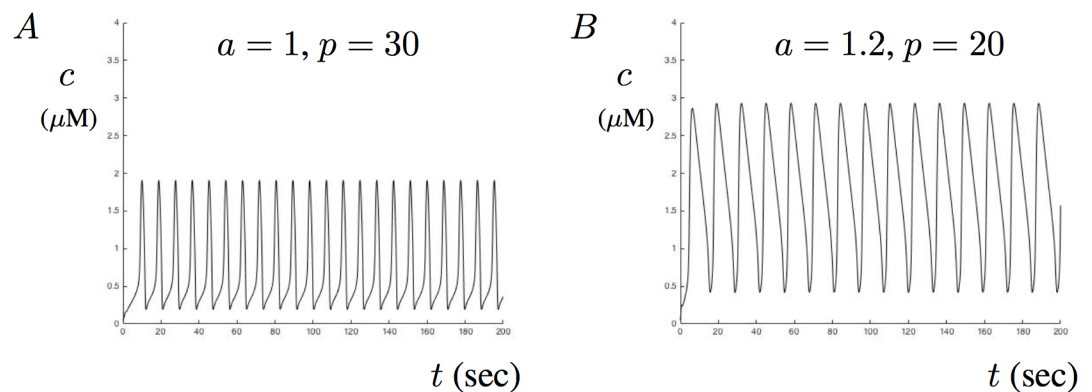


**Fig 6. Effects of $a$ and $p$ on Ca$^{2+}$ oscillation amplitudes.** This figures shows two examples of sustained Ca$^{2+}$ oscillations for two sets of parameter selections of $a$ and $p$. A shows Ca$^{2+}$ oscillations with peak amplitudes around 2 corresponding to $a = 1$ and $p = 30$. B shows similar oscillations with peak amplitude closer to 3 corresponding to $a = 1.2$ and $p = 20$.

https://doi.org/10.1371/journal.pone.0202503.g006

**Contribution of Aβ on calcium signaling through the ryanodine receptor.** To better understand the influence of Aβ on Ca²⁺ signaling, we now turn our attention to the contributions of the RyR. Recall that in our model we assume that Aβ affects the RyR by altering the receptor's sensitivity for CICR. To determine the specific contribution of this altered sensitivity, we first simulate the model for fixed $a$ and $p$ and describe the dynamics of varying the parameter $k_a$. Our simulations show that in the presence of Aβ, changing the parameter $k_\alpha$ can produce aberrant Ca²⁺ signals. These aberrant signals result as transitions through MMOs for fixed Aβ levels. However, we also show that we can control these signals by increasing $k_2$, the maximal kinetic rate of the RyR.

Fig 7 shows four Ca²⁺ traces with $k_\alpha = 0.5$, $0.9$, $1$, and $1.25$ when $a = 0.25$ and $p = 10$ are fixed. Notice that for $k_\alpha = 1$ aberrant Ca²⁺ signals emerge. Also included in Fig 7A is the corresponding partial bifurcation diagram for $a = 0.25$ using $k_\alpha$ as the bifurcation parameter. Notice that MMOs exist for a large parameter set of $k_\alpha$. In Fig 7A there are four period doubling bifurcations that each have been labeled as PD. These occur around the parameter values of $k_\alpha = \{0.5893, 0.7599, 1.01, 1.026\}$, respectively. The single Hopf bifurcation occurs around the parameter value $k_\alpha = 1.313$. The bifurcation diagram in A provides us with a way to predict the Ca²⁺ signals for a large set of the parameter $k_\alpha$. Notice that stable periodic solutions occur for the parameter intervals $k_{\alpha s} = (0, 0.5893) \cup (1.026, 1.313)$. We have MMOs for the parameter interval $k_{\alpha mmo} = (0.5893, 1.026)$ with various sub-threshold oscillations patterns. Fig 7D shows aberrant Ca²⁺ signals as the parameter $k_\alpha$ remains close to the period doubling value 1.01. Fig 7E shows small stable periodic oscillations for the value $k_\alpha = 1.25$ near the Hopf point.

Each trace illustrated in Fig 7 shows a different type of Ca²⁺ response based on the value of $k_\alpha$. One possible way of dealing with the aberrant signals and MMOs is to drive the maximal reaction rate of the RyR up. This corresponds to increasing the value of $k_2$ in the model. Fig 8A shows a two-parameter bifurcation diagram with $k_\alpha$ on the $x$-axis and $k_2$ on the $y$-axis. What
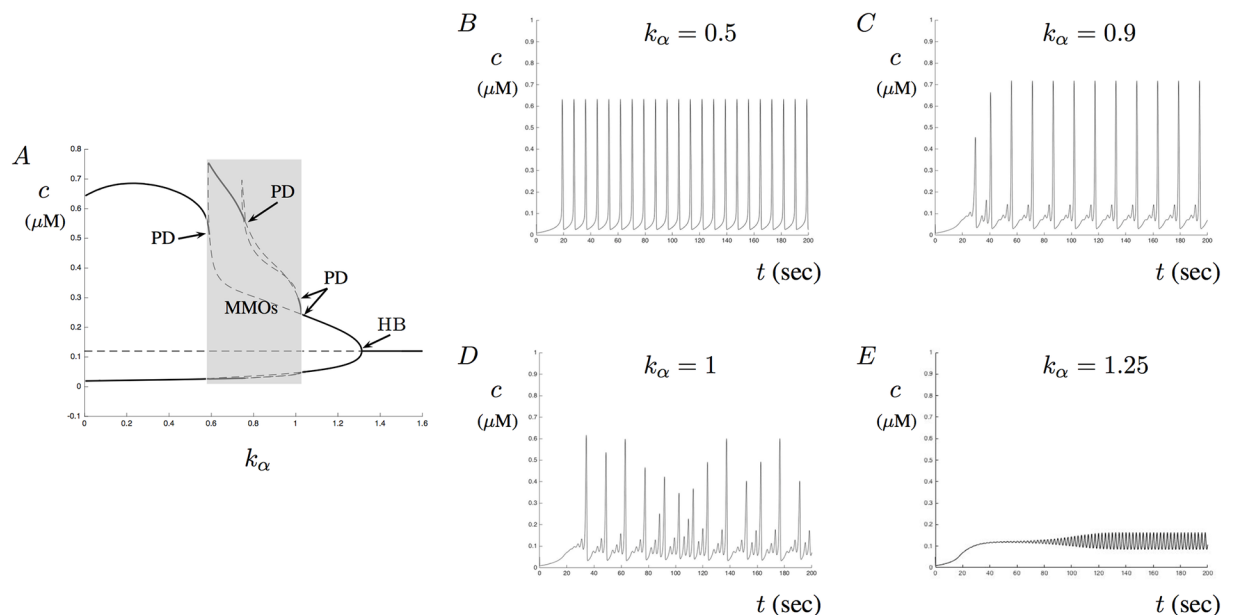


**Fig 7. The effects of $k_\alpha$ on Ca²⁺ signals in the presence of Aβ.** This figure shows a bifurcation diagram and four Ca²⁺ traces. A shows a partial bifurcation diagram for the parameter $k_\alpha$. In this figure, a number of period doubling points have been labeled as PD. The shaded region corresponds to MMOs. The single Hopf bifurcation point has been labeled with HB. B-E show four solutions for the parameter values $k_\alpha = 0.5$, 0.9, 1, and 1.25, respectively. D shows aberrant Ca²⁺ signals.
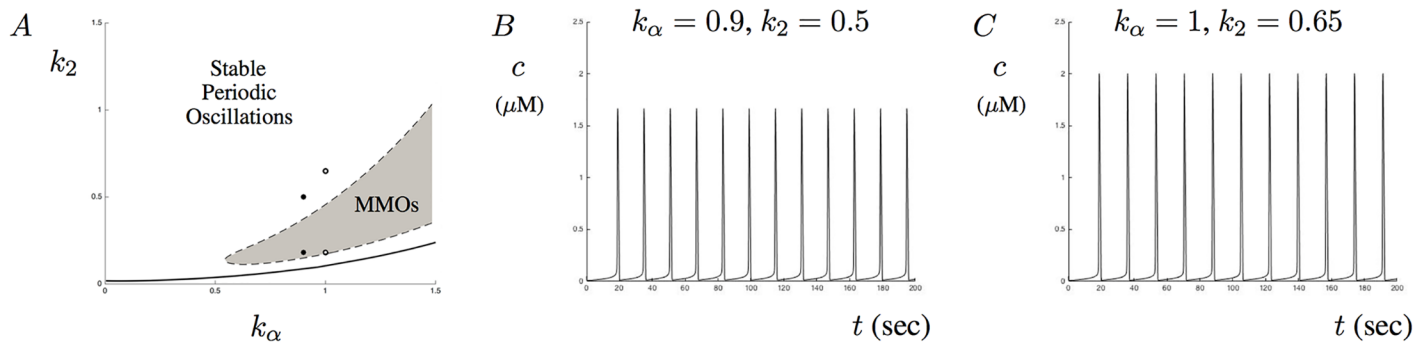
**Fig 8. Changing the maximal reaction rate of the RyR.** This figures shows the effects of changing the parameter $k_2$ on model solutions. A shows a two parameter bifurcation diagram with $k_\alpha$ and $k_2$ as the bifurcation parameters. The shaded region corresponds to the region of MMOs. The solid curve corresponds to the manifold of Hopf bifurcation points. The two dots on the left side represents the locations of the parameter values of $k_2$ used to generate the Ca$^{2+}$ traces in Fig 7C and Fig 8B. The two dots on the right side represents the locations of the parameter values of $k_2$ used to generate the Ca$^{2+}$ traces in Fig 7D and Fig 8C. B and C show the stable periodic oscillations that occur when $k_2$ is increased to $k_2 = 0.5$ and $k_2 = 0.65$, respectively.

this diagram illustrates is the region of MMOs produced by the model for the parameter ranges of $k_\alpha$ and $k_2$ given in the figure. Suppose that for a fixed $k_\alpha$ value, Ca$^{2+}$ signals undergo aberrant signals or MMOs. By increasing the parameter $k_2$ sufficiently, passage into stable periodic solutions will occur. This suggests that the maximal rate of the RyR kinetics may help to control both aberrant Ca$^{2+}$ signals and MMOs. To see this, Fig 8B shows the solution corresponding to those in Fig 7C with $k_\alpha = 0.9$ when $k_2 = 0.18$ is increased to $k_2 = 0.5$. Similarly, Fig 8C shows the solution corresponding to those in Fig 7D with $k_\alpha = 1$ when $k_2 = 0.18$ is increased to $k_2 = 0.65$. Notice that although solutions do settle into stable periodic orbits that the amplitude of the signals increase. Thus, increasing the parameter $k_2$ may help to stabilizes aberrant oscillations at the cost of increasing Ca$^{2+}$ oscillation amplitude. A similar stable region also exists below the region of MMOs. This region would also help control signals but may be more difficult to precisely isolate the appropriate range of $k_2$.

**Dynamic levels of IP$_3$ with no membrane potential.** The model dynamics exhibited in the figures above are triggered by a constant value of IP$_3$ in the cytosol. Recall that *in vivo*, IP$_3$ production is typically a result of an agonist activated G-couple protein. The rates of IP$_3$ production and degradation are both modulated by intracellular Ca$^{2+}$, and as such, the release of Ca$^{2+}$ through the IP$_3$ receptor can directly alter the IP$_3$ signaling pathway. Furthermore, there is growing evidence that A$\beta$ also affects the IP$_3$ signaling pathway [7]. Thus, we extend our model to include a dynamic variable for IP$_3$ production and degradation, and look to include the influence of A$\beta$ on this signaling mechanism when $p_s = 0$. More specifically, we include an additional equation for IP$_3$ and model the influence of A$\beta$ on the production of IP$_3$.

We make use of the hybrid model formulated by Politi et al. (2006) to track IP$_3$ production and degradation. Their model takes the form

$$\tau_p \frac{dp}{dt} = V_{PLC} \frac{c^2}{K_{PLC}^2 + c^2} - \left( \frac{\eta c^2}{K_{3K}^2 + c^2} + (1 - \eta) \right) p, \tag{20}$$

where

$$\tau_p = \frac{1}{k_{3K} + k_{5P}}, \quad \text{and} \quad \eta = \frac{k_{3K}}{k_{3K} + k_{5P}}.$$

The first term on the right hand side of (20) corresponds to the production of IP$_3$ and the second term is the degradation. In (20), $V_{PLC}$ is the maximal production rate, $K_{PLC}$ characterizes

the sensitivity of PLC, $K_{3K}$ is the half saturation constant for the degradation term. The constants $k_{3K}$ and $k_{5P}$ correspond to the IP$_3$ phosphorylation and dephosphorylation rates, respectively. $K_{PLC}$ and $\eta$ are parameters used to adjust the positive and negative feedback of Ca$^{2+}$, respectively. One of the advantages for using this hybrid model is that it can easily be altered to reproduce both class I and class II mechanisms (see [18] for details). Another advantage, is that this model breaks the IP$_3$ process into two components: a production and a degradation. This will make it easier for us to incorporate the effects of A$\beta$ on the IP$_3$ production process.

In their experiment, Demuro and Parker (2013) showed that introducing A$\beta$ directly into *Xenopus* oocytes causes an increase in Ca$^{2+}$ dependent fluorescence (a measure for the amount of intracellular Ca$^{2+}$). Even though their experiments are in oocytes, the ubiquitous properties of IP$_3$ signaling may make their results relevant to other cells including neurons. Their findings suggest that A$\beta$ does not interact directly with the IP$_3$ receptor, but instead they propose that intracellular Ca$^{2+}$ liberation evoked by A$\beta$ involves opening of IP$_3$ receptors as a result of stimulated production of IP$_3$ via G-protein-mediated activation of PLC. As such, in the presence of A$\beta$, IP$_3$ are actively stimulated and persist for many minutes or hours even though IP$_3$ is metabolized within tens of seconds [58]. Based on these findings, we assume that $V_{PLC}$ takes the form

$$V_{PLC} = v_{PLC} + \mu_{PLC}a, \tag{21}$$

and $K_{PLC}$ can be written similarly as

$$K_{PLC} = k_{PLC} + \kappa_{PLC}a, \tag{22}$$

where the parameters $\mu_{PLC}$ and $\kappa_{PLC}$ control the strength of the linear influence of A$\beta$ on each term, respectively. For our purposes, we set both of these values to be $\mu_{PLC} = \kappa_{PLC} = 1$. Thus, we add the following equation to (18) and (19) and look to determine the impact of A$\beta$ on model solutions

$$\tau_P \frac{dp}{dt} = (v_{PLC} + \mu_{PLC}a)\frac{c^2}{(k_{PLC} + \kappa_{PLC}a) + c^2} - \left(\frac{\eta c^2}{K_{3K}^2 + c^2} + (1 - \eta)\right)p. \tag{23}$$

In our simulation we use the work of [59] to set a number of parameter values. However, we assume that both positive and negative feedback are present simultaneously and as such make parameter adjustments as needed. The parameter values that we use for our simulations are given in Table 2. With these additional contributions, we now have a model that includes the impact of A$\beta$ on multiple Ca$^{2+}$ signaling mechanisms. Although the model has a large number of variables and parameters, we seek to characterize model solutions by investigating the dynamical properties of the model in the presence of A$\beta$.

In the absence of A$\beta$, model solution with initial condition for IP$_3$ = 0.01 shows a small Ca$^{2+}$ influx followed by a transition to it's steady-state level close to 0.5 $\mu$M. This is consistent with what we expect as the amount of IP$_3$ is dynamic and depends on Ca$^{2+}$. It will take sometime for enough IP$_3$ to be present in order to trigger a signaling event throught the receptor. Fig 9A and 9B show the model solution for Ca$^{2+}$ and IP$_3$, respectively in the absence of A$\beta$. Notice that the amount of IP$_3$ also reaches a steady-state level.

**Table 2. Parameter values of the IP$_3$ model (23).**

| IP$_3$ parameters | | | | | |
|---|---|---|---|---|---|
| $v_{PLC}$ | 1.5 $\mu$M s$^{-1}$ | $k_{5P}$ | 0.25 s$^{-1}$ | $K_{3K}$ | 0.4 $\mu$M |
| $k_{PLC}$ | 1 $\mu$M | $k_{3K}$ | 0.5 s$^{-1}$ | | |
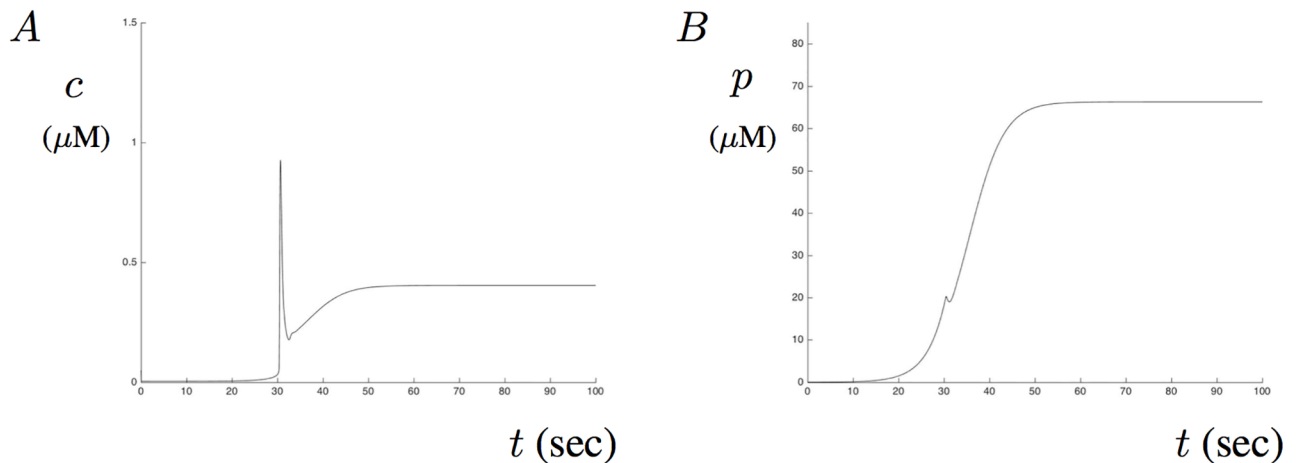
**Fig 9. Dynamic IP$_3$ without A$\beta$.** A shows Ca$^{2+}$ and B shows IP$_3$ as a function of time in the absence of A$\beta$. A spike of Ca$^{2+}$ occurs once enough IP$_3$ has accumulated but does not lead to sustained oscillations. The amount of IP$_3$ settles to a steady-state level in B.

https://doi.org/10.1371/journal.pone.0202503.g009

Since we are interested in understanding the potential effect of A$\beta$ on Ca$^{2+}$ signals, we use $a$ as a bifurcation parameter and investigate model solutions. Fig 10A shows a partial bifurcation diagram with $a$ as the bifurcation parameter. This diagram has two oscillatory regions separated by a region of a single stable-steady state. The four Hopf bifurcations are labeled along with a number of period doubling points. Notice that there are four regions of MMOs (shaded regions) that appear close to each Hopf point. In addition to the Hopf bifurcation points, four period doubling points have also been labeled with two limit points (LP). We provide the value of each of these points in Table 3 and use them to identify solution patterns. As the parameter
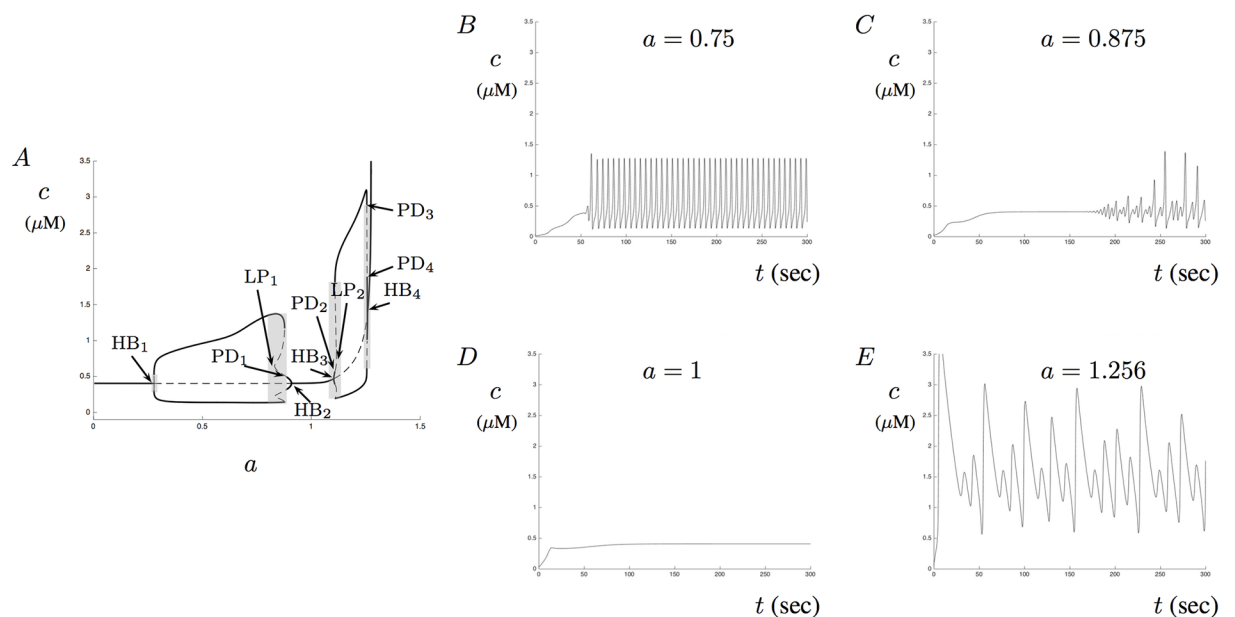


**Fig 10. Calcium signals in the presence of A$\beta$ with dynamic IP$_3$.** This figure shows a bifurcation diagram and four Ca$^{2+}$ traces for the model with dynamic IP$_3$. A shows a partial bifurcation diagram where two oscillatory regions are separated by a single steady-state region. The shaded regions near each of the four Hopf bifurcations correspond to MMOs. Numerous period doubling bifurcations occur around the shaded regions. Two important limit points have been labeled LP$_1$ and LP$_1$. These points are important in the description of solutions. B-D show model solutions for $a$ = 0.75, 0.875, 1, and 1.256, respectively. The various patterns in these figures are predicted by the bifurcation diagram in A.

https://doi.org/10.1371/journal.pone.0202503.g010

**Table 3. Solution behavior for model with dynamic IP$_3$.**

| Parameter $a$ interval | Point type | Description of solution pattern |
|---|---|---|
| (0, 0.2783) | (0, HB$_1$) | Stable steady-state solutions |
| (0.2783, 0.8318) | (HB$_1$, LP$_1$) | Stable periodic solutions |
| (0.8318, 0.8857) | (LP$_1$, PD$_1$) | Mixed-mode oscillations |
| (0.8857, 0.909) | (PD$_1$, HB$_2$) | Stable periodic solutions with small amplitude |
| (0.909, 1.103) | (HB$_2$, HB$_3$) | Stable steady-state solutions |
| (1.103, 1.109) | (HB$_3$, PD$_2$) | Stable periodic solutions with small amplitude |
| (1.109, 1.16) | (PD$_2$, LP$_2$) | Mixed-mode oscillations |
| (1.16, 1.255) | (LP$_2$, PD$_3$) | Stable periodic solutions with large amplitude |
| (1.255, 1.256) | (PD$_3$, PD$_4$) | Mixed-mode oscillations with elevated Ca$^{2+}$ levels |
| (1.256, 1.257) | (PD$_4$, HB$_4$) | Stable periodic solutions with small amplitude but with elevated Ca$^{2+}$ levels |
| (1.257, 1.274) | (HB$_4$, LP$_3$) | Stable high Ca$^{2+}$ steady-state solutions |

https://doi.org/10.1371/journal.pone.0202503.t003

$a$ increases to LP$_3$ = 1.274, solutions become unphysical. Thus, we limit our investigation for values of $a$ between 0 and 1.274. Fig 10B–10D show Ca$^{2+}$ traces predicted by Fig 10A for various values of $a$. Notice that aberrant signals are also present for the model with a dynamic equation for IP$_3$.

## Calcium model with influence of membrane potential

In our simulations below, we examine the effects of changes to membrane potentials by first incorporating the membrane into the model and by stimulating the membrane with a constant applied current pulse. The impact of such an applied current on the voltage $V$ and the resulting Ca$^{2+}$ current are shown in Fig 11. A stimulating current of 300 nA applied for $t = 0.1$ seconds initiated at $t = 2$ generates the potential response shown in Fig 11A. Fig 11B and 11C show the response due to an applied stimulus lasting for one and ten seconds, respectively. These changes in membrane potential cause the inward currents through the VGCC illustrated in Fig 11D–11F, for $t = 0.1$, $t = 1$, and $t = 10$ seconds, respectively. Notice that in Fig 11C the membrane voltage saturates as the duration of the applied current is increased. Although the mechanisms for generating these signals is fairly simplistic, our results align well with experimental data showing similar saturating levels in astrocytes [38]. The effects of the inward Ca$^{2+}$ through the VGCC are included in the flux term $J_{vca}$ and as such, allows us to study the impact of membrane potentials on Ca$^{2+}$ signals. In all subsequent figures, we have applied a constant current pulse at $t = 100$ for a duration of 50 seconds. Such an applied current does not capture an *in vivo*-like representation of membrane potentials, but it does offer a way to link the model with typical voltage clamp experiments where the amplitude and duration of the applied current can be controlled.

To investigate the impact of a constant current pulse on Ca$^{2+}$ signaling, we first simulate (18) and (19) with constant values of IP$_3$. In these simulations we set $p_s = 1$ and plot Ca$^{2+}$ concentrations as a function of time. Tracking the membrane potential and including it into the model will have an effect on Ca$^{2+}$ signals. Specifically, the membrane will alter the dynamics of the effect of $p$ on model solutions. In order to illustrate this point we have plotted the model responses when no A$\beta$ is present for various values of $p$ in Fig 12. When these solutions are compared to Fig 2, we can see that the inclusion of the membrane potential increases the response frequency and MMOs occur for smaller values of $p$ (for example $p = 13$ here instead of $p = 17$ in Fig 2).

Notice that in Fig 12D–12F Ca$^{2+}$ signals seem to stabilize in single-mode oscillations upon the release of the stimulus before transitioning back into MMOs. This may provide one
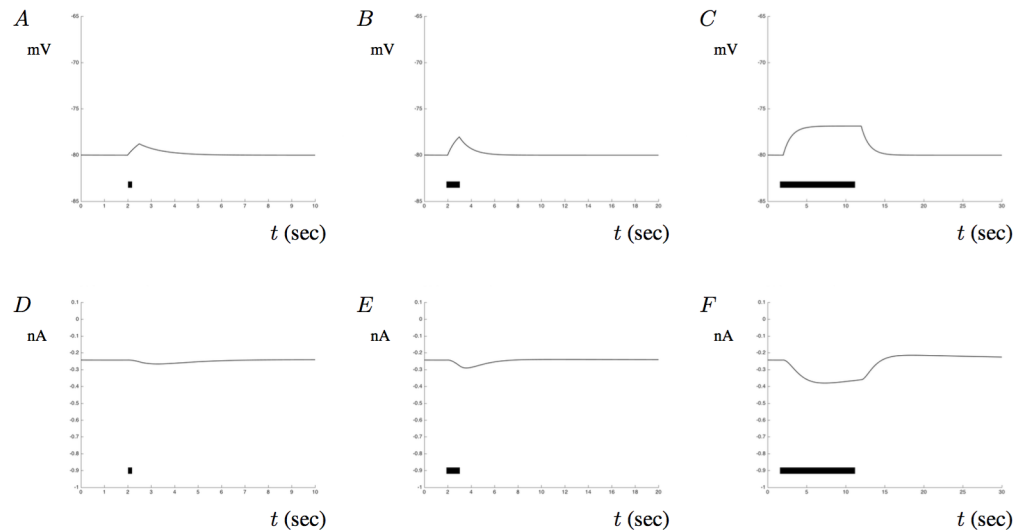
**Fig 11. Ca$^{2+}$ flux due to changes in membrane potential.** This figures shows the Ca$^{2+}$ current $I_{ca}$ in response to changes in membrane potential. A-C show changes in the membrane potential of the astrocytic model when a current of 300 nA is applied for a duration of 0.1 second (A), 1 second (B), and 10 seconds (C). The current was applied at $t = 2$ seconds and is represented by the black bar at the bottom of each figure. D-F show the corresponding VGCC current $I_{ca}$ as defined by (15).

https://doi.org/10.1371/journal.pone.0202503.g011

possible path for stabilizing Ca$^{2+}$ signaling. In an *in-vivo* like environment, membrane potentials vary based on intrinsic response mechanisms to a stimulus. Our results show that artificially triggering membrane stimulation could potentially help to stabilize Ca$^{2+}$ signals. Furthermore, Fig 12E shows that the model solution can exhibit a large number of sub-threshold oscillations before triggering a larger spike. This type of MMO is different from those
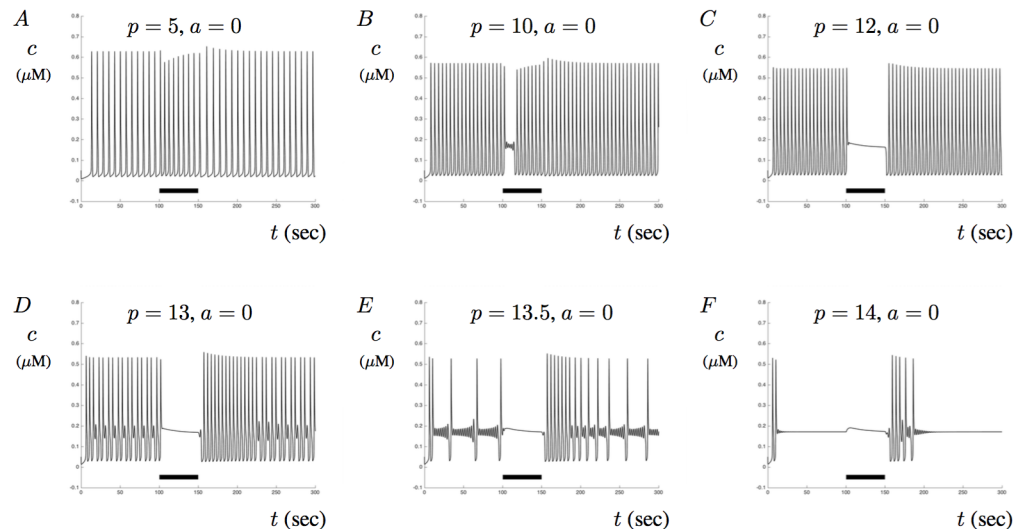


**Fig 12. The influence of IP$_3$ on Ca$^{2+}$ signals with membrane potential.** This figures shows the impact of membrane potential on Ca$^{2+}$ signaling. In each figure, membrane potentials are included as a response to a sustained applied current of 300 nA lasting from $t = 100$ to $t = 150$. Figs A, B, and C show intracellular Ca$^{2+}$ signals when $p = 5$, $p = 10$, and $p = 12$ with $a = 0$, respectively. Figs D, E, and F show the response when $p = 13$, $p = 13.5$, and $p = 14$, respectively. Note that the inclusion of the membrane potential filters MMOs and can help establish transient single-mode oscillations upon the termination of the applied current (D,E).

https://doi.org/10.1371/journal.pone.0202503.g012
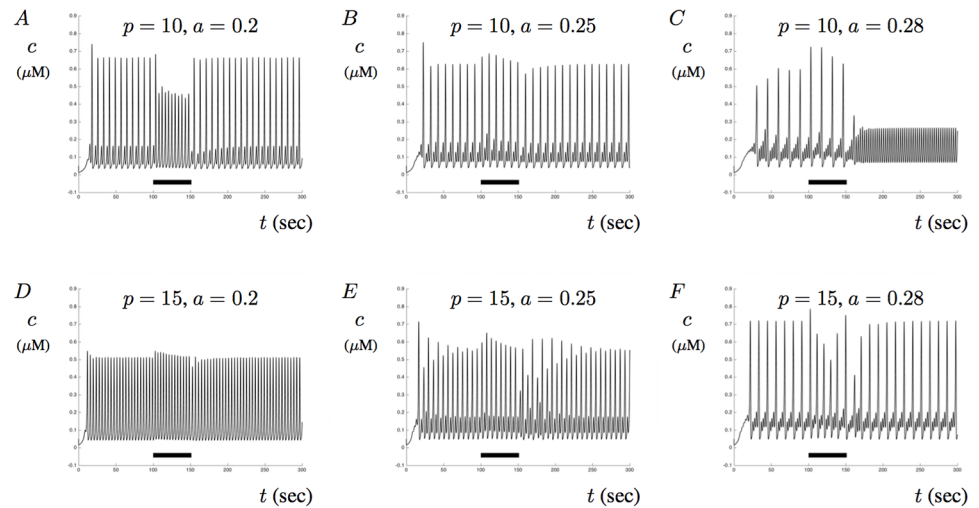
**Fig 13. The influence of A$\beta$ on Ca$^{2+}$ signals with membrane potential.** This figures shows the impact of membrane potential on Ca$^{2+}$ signaling. In each figure, changes in membrane potential are included as a response to a sustained applied current of 300 lasting from $t = 100$ to $t = 150$. Figs A, B, and C show intracellular Ca$^{2+}$ signals when $p = 10$ and when $a = 0.2$, $a = 0.25$, and $a = 0.28$, respectively. Figs D, E, and F show the response when $p = 15$ and when $a = 0.2$, $a = 0.25$, and $a = 0.28$, respectively.

https://doi.org/10.1371/journal.pone.0202503.g013

illustrated previously and shows that membrane potentials can have an impact on global Ca$^{2+}$ signals and play an important role in Ca$^{2+}$ regulation. A full analysis for understanding these transitions is beyond the scope of this work but could prove useful for predicting how membrane stimulation may be used to control and/or stabilize aberrant Ca$^{2+}$ signals.

Model solution patterns are not only linked to the amount of IP$_3$ and the inclusion of membrane potential, but also by the amount of A$\beta$ present in the model. To better understand the roles of IP$_3$, membrane potentials, and A$\beta$ on Ca$^{2+}$ signaling, we simulate the model and provide the solutions when $p = 10$ and $p = 15$ with various levels of A$\beta$ for $p_s = 1$. Illustrated in Fig 13 are six model solutions that illustrate the impact of A$\beta$ and membrane potentials on Ca$^{2+}$ signaling. When $p = 10$ is fixed and $a$ is altered, model behavior is directly impacted by the application and removal of a constant current pulse. This is illustrated in Fig 13A–13C where $a = 0.2$, $a = 0.25$, and $a = 0.28$. Specifically, Fig 13C shows that upon the termination of the applied stimulus, Ca$^{2+}$ signals do not go back to MMO patterns but instead transition to stable single-mode oscillations. This shows that stimulation of the membrane can alter intrinsic dynamical patterns and be used to stabilize various types of Ca$^{2+}$ signals. Fig 13D–13F show model solutions for $p = 15$ with $a = 0.2$, $a = 0.25$, and $a = 0.28$, respectively. It is interesting to note that when we apply a constant current pulse, Ca$^{2+}$ solutions can transition into steady MMOs as the level of A$\beta$ increased towards $a = 0.28$. Although we do not analyze the bifurcation structure, the inclusion of membrane potentials in the model appears to have altered the parameter dependance where regions of MMOs can occur as well as transitions from single-to mixed-mode oscillations. Further analysis may be beneficial for drawing out the underlying mechanisms in the stable oscillatory patterns when a constant current is applied in the model.

Because the impact of membrane potentials are controlled by $p_s$, we have also provided model simulations when this parameter is altered. Small values of $p_s$ correspond to small influence of membrane potential while larger values can be used drive the amplitude of Ca$^{2+}$ signals. Fig 14 shows four simulations for four different values of $p_s$. When $p_s = 0.5$, Fig 14A shows that the effects of membrane potentials are small and no significant changes in Ca$^{2+}$ are observed other than a slight increase in the subtreshold oscillations. When $p_s = 0.75$, Fig 14B
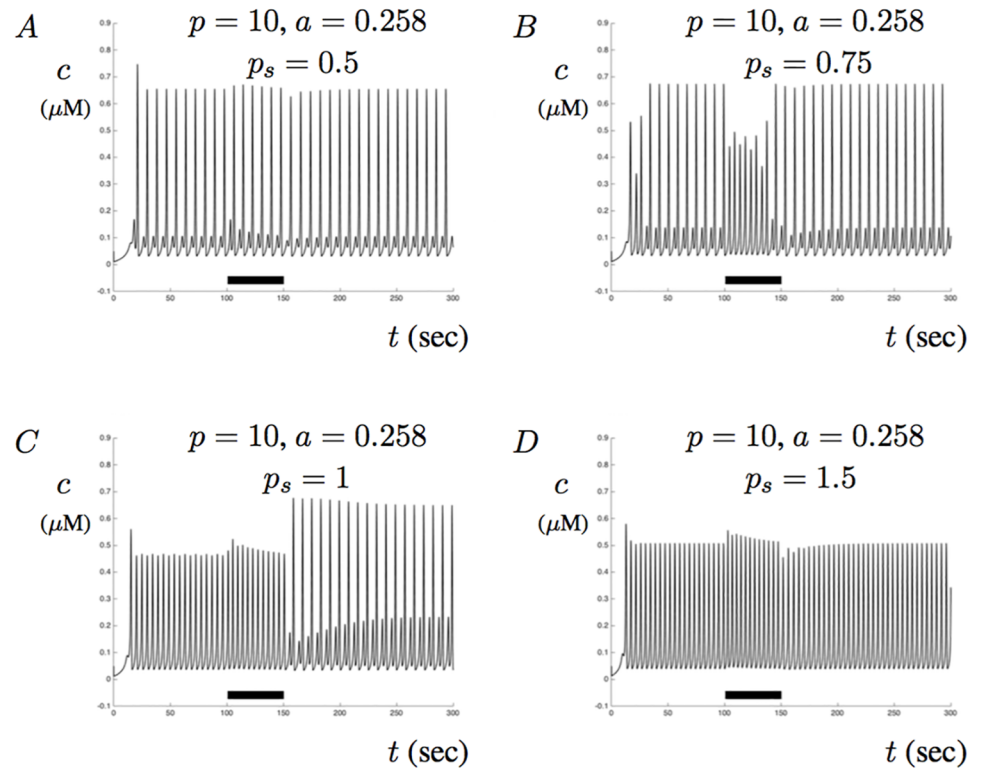
**Fig 14. The impact of scaling $I_{ca}$ on model solutions.** This figures shows various model solutions when the scaling parameter $p_s$ is altered. In each figure, $p = 10$, and the amount of A$\beta$ is fixed at $a = 0.258$. A-D show the response of (18) and (19) when $p_s = 0.5$, $p_s = 0.75$, $p_s = 1$, and $p_s = 1.5$, respectively. Notice that B shows that Ca$^{2+}$ can enter aberrant oscillatory patterns when the membrane is stimulated by a constant applied current. C shows that Ca$^{2+}$ signals can enter MMOs with altered amplitudes when the applied current stimulus is turned off.

https://doi.org/10.1371/journal.pone.0202503.g014

suggests that the effects of membrane potentials are large enough to alter the amplitude of Ca$^{2+}$ oscillations during the applied current. Fig 14C shows that when $p = 1$, contributions from membrane potentials increase overall Ca$^{2+}$ signaling amplitude. With these values of $p$ and $a$, the solution transitions from single mode oscillations with amplitude around 0.45 to MMO with an increased amplitude to around 0.7. Fig 14D shows that a large influence of membrane potentials (when $p = 1.5$) does not alter the signal amplitude or oscillatory mode significantly.

Although much analysis remains to fully understand the dynamics of the model, the results of our simulations suggest that A$\beta$ can alter Ca$^{2+}$ regulatory mechanisms in a way that leads to both MMOs and aberrant signaling. We have shown that bifurcation regions for dynamical transitions from single mode to MMOs can increase in the presence of A$\beta$. By altering RyR receptor dynamics, we show that transitions from MMO back to single-mode oscillations can occur. Furthermore, we show that stimulation of the membrane can also be used to control various types of Ca$^{2+}$ signals. Although we have made a number of simplifying assumptions in the model development, our approach can be easily altered to include other more complex interactions and mechanisms that influence Ca$^{2+}$ regulation.

## Discussion

Intracellular Ca$^{2+}$ is a critically important second messenger within the nervous system. In neurons, Ca$^{2+}$ is known to mediate the signaling pathways that control neurotransmitter

release, gene expression, metabolism, plasticity, development, proliferation, and cell death [60]. As such, $Ca^{2+}$ may play a major role in the pathogenesis of AD. Unfortunately, the complexity of $Ca^{2+}$ signaling makes it difficult to precisely understand how A$\beta$ impacts different intracellular regulation mechanisms and components. Various studies have decoupled particular components and merging these theories together to form a whole-cell computational model can help us better understand intracellular $Ca^{2+}$ regulation and what leads to aberrant signaling. One of our goals is to model $Ca^{2+}$ in a simplified whole-cell environment that has predictable qualitative structure so that we can study the effects of A$\beta$ on the dynamics. As such, the qualitative features described in this study give us a way to track $Ca^{2+}$ patterns using dynamical systems theory.

The simulations presented in this study occur on the order of seconds to minutes while the progression of AD occurs on the timescale of months to years. However, in our model we are using the accumulation of A$\beta$ to describe the potential stage in the evolution of AD. Even before toxic A$\beta$ plaques can aggregate, the slow accumulation of A$\beta$ peptides can trigger alterations in $Ca^{2+}$ signaling patterns. Our model shows that aberrant signals and changes in homeostasis levels can emerge as the amount of A$\beta$ is increased. In an *in vivo* environment these changes may be subtle and actually evolve over days or months. Any alterations in intracellular $Ca^{2+}$ homeostasis can affect the apoptotic signaling cascade. Both the mitochondria and the ER play a significant role in apoptosis and are sensitive to changes in $Ca^{2+}$ levels. Although we have not considered mitochondrial effects, we do track ER $Ca^{2+}$. Further analysis that looks at the time evolution of $c_e$ could be useful in predicting chronic changes of $Ca^{2+}$ homeostasis in AD.

Developing a whole-cell $Ca^{2+}$ model that has predictable qualitative structure in the presence of A$\beta$ is challenging. Although A$\beta$ influences many $Ca^{2+}$ regulatory mechanisms, the particular way which A$\beta$ affects these mechanisms is generally not known. Additionally, the temporal influence of A$\beta$ on certain mechanisms could occur on the order of milliseconds, seconds, days, months, or years. As such, any computational model will necessarily make a number of simplifying assumptions. Even by exploiting these simplifications, our model includes a large number of parameters that make mathematical analysis limited. Unfortunately, we do not have robust estimates for many of the parameters involved in the model. However, we have attempted to provide justification for many assumptions and parameter choices based on the literature and the experimental data currently available. We do recognize that many of these assumptions may need to be altered as we continue to improve our understanding of the effects of A$\beta$ in an AD environment.

The ubiquitous nature of the $Ca^{2+}$ regulatory mechanisms used in our model makes it easily adaptable for studying various cell types with spatial components. Specifically, A$\beta$ has been shown to cause complex $Ca^{2+}$ signals in astrocytes [61, 62]. In these astrocytes, $Ca^{2+}$ waves and oscillations signals can occur on timescales even slower than those typical of other non-excitable neuroglia. Although our modeling approach does not include spatial components, additional mechanisms can be constructed to account for wave generating behaviors. Furthermore, astrocytes can facilitate synaptic transmission and plasticity through the uptake of neurotransmitter [63] and complex models between neurons and astrocytes have been developed to study these interactions [38, 64, 65]. Both microglia and astrocytes have been described as modulators for A$\beta$ clearance and degradation [66] and our approach may be useful for better understanding these mechanisms.

It is clear that A$\beta$ plays an essential role in the cognitive decline in AD by directly affecting synaptic transmission [11, 67–70]. However, synaptic transmission is typically precipitated by a presynaptic potential which allows $Ca^{2+}$ ions to flow into the cell through VGCC. The contributions of fast local $Ca^{2+}$ signals with slow global $Ca^{2+}$ patterns, especially under the influence

of A$\beta$, may help explain why breakdowns in synaptic efficacy can occur in an AD environment [11, 45, 67, 69, 71, 72]. The accumulation or presence of A$\beta$ may directly, or indirectly, impact various Ca$^{2+}$ driven mechanisms during synaptic transmission. The simplified whole-cell Ca$^{2+}$ model presented here could be linked with a synaptic Ca$^{2+}$ model to investigate how global aberrant Ca$^{2+}$ signals may impact synaptic transmission on multiple timescales. Simulations over long timescales may help explain how slow global whole-cell Ca$^{2+}$ signals interfere with fast local Ca$^{2+}$ signals at the synapse.

Different individual models exist for the various signaling components used in our simplified whole-cell model development. For example, we used the Sneyd and Dufour (2002) formulation for the IP$_3$ receptor model. Although this model is sound and well-suited for our purposes, it does increase the number of necessary variables considerably. One could use a two equation model for IP$_3$ (such as those described in [26, 73]), but the number of parameters will remain large. Similarly, alternative models for the RyR may tease out alternative conclusions when influenced by A$\beta$ (such as using a model as in [74]). As such, we encourage further development of the model as experimental data becomes available. Matching model dynamics with experimentally recorded data can help select the component model best suited for the particular study.

Our model solutions are highly sensitive to certain parameters and the oscillatory responses presented here only occur under certain scenarios. Because of the complexity of Ca$^{2+}$ regulation along with understanding the impact of A$\beta$, any computational model would benefit from both local and global sensitivity analysis. Although we have not performed any sensitivity analysis, we do understand that much of the analysis and many of our conclusions may be valid for a small set of parameters. Further, the sensitivity of a particular parameter may influence how the model transitions into aberrant Ca$^{2+}$ signals. As such, we recommend that sensitivity analysis be performed as a next step in order to better understand the role of parameters on model dynamics.

In conclusion, we have shown that aberrant Ca$^{2+}$ signals can occur in a simplified whole-cell model under the influence of A$\beta$. Furthermore, we showed that regions of MMOs can expand as a consequence of increasing the amount of A$\beta$ in the model. This may partially explain how Ca$^{2+}$ signals are impacted by A$\beta$ from a dynamics perspective within an *in vivo* like environment. Continued refinement of the model in conjunction with experimental data matching will help make the model more useful. In turn, this can help us determine how to control for both aberrant signals and increased homeostasis Ca$^{2+}$ levels. The model can then be used to better understand the impact of A$\beta$ on Ca$^{2+}$ fluxes through individual regulatory components (such as IP$_3$, RyR, and plasma membrane). This computational model can help us study complex cellular behavior in an AD environment by tracking the influence of many interconnected biological mechanisms.

## Supporting information

**S1 Appendix. A summary of both the IP$_3$ receptor model equations and those governing the membrane potential.** Also provided in the appendix are the model parameters used in the Hodgkin and Huxley formulation of the membrane potential.
(PDF)

## Acknowledgments

## Author Contributions

**Investigation:** Joe Latulippe, Derek Lotito.

**Methodology:** Joe Latulippe, Derek Lotito, Donovan Murby.

**Software:** Joe Latulippe, Donovan Murby.

**Visualization:** Joe Latulippe.

**Writing – original draft:** Joe Latulippe, Derek Lotito.

**Writing – review & editing:** Donovan Murby.

## References

1. Alzheimer's Association. 2016 Alzheimer's disease facts and figures. Alzheimers Dement. 2016; 12(4):459–509. https://doi.org/10.1016/j.jalz.2016.03.001 PMID: 27570871

2. Gouras GK, Tsai J, Naslund J, Vincent B, Edgar M, Checler F, et al. Intraneuronal A$\beta$42 Accumulation in Human Brain. The American Journal of Pathology. 2000; 156(1):15–20. https://doi.org/10.1016/S0002-9440(10)64700-1 PMID: 10623648

3. Oddo S, Caccamo A, Smith IF, Green KN, LaFerla FM. A dynamic relationship between intracellular and extracellular pools of A$\beta$. Am J Pathol. 2006; 168(1):184–94. https://doi.org/10.2353/ajpath.2006.050593 PMID: 16400022

4. Ferreiro E, Oliveira CR, Pereira C. Involvement of endoplasmic reticulum Ca$^{2+}$ release through ryanodine and inositol 1,4,5-triphosphate receptors in the neurotoxic effects induced by the amyloid-$\beta$ peptide. J Neurosci Res. 2004; 76(6):872–80. https://doi.org/10.1002/jnr.20135 PMID: 15160398

5. Kuchibhotla KV, Goldman ST, Lattarulo CR, Wu HY, Hyman BT, Bacskai BJ. A$\beta$ plaques lead to aberrant regulation of calcium homeostasis in vivo resulting in structural and functional disruption of neuronal networks. Neuron. 2008; 59(2):214–25. https://doi.org/10.1016/j.neuron.2008.06.008 PMID: 18667150

6. Demuro A, Mina E, Kayed R, Milton SC, Parker I, Glabe CG. Calcium dysregulation and membrane disruption as a ubiquitous neurotoxic mechanism of soluble amyloid oligomers. J Biol Chem. 2005; 280(17):17294–300. https://doi.org/10.1074/jbc.M500997200 PMID: 15722360

7. Demuro A, Parker I. Cytotoxicity of intracellular A$\beta$ 42 amyloid oligomers involves Ca$^{2+}$ release from the endoplasmic reticulum by stimulated production of inositol trisphosphate. J Neurosci. 2013; 33(9):3824–33. https://doi.org/10.1523/JNEUROSCI.4367-12.2013 PMID: 23447594

8. Lopez JR, Lyckman A, Oddo S, Laferla FM, Querfurth HW, Shtifman A. Increased intraneuronal resting [Ca$^{2+}$] in adult Alzheimer's disease mice. J Neurochem. 2008; 105(1):262–71. https://doi.org/10.1111/j.1471-4159.2007.05135.x PMID: 18021291

9. Hardy J, Allsop D. Amyloid deposition as the central event in the aetiology of Alzheimer's disease. Trends Pharmacol Sci. 1991; 12(10):383–8. https://doi.org/10.1016/0165-6147(91)90609-V PMID: 1763432

10. Hardy J, Selkoe DJ. The amyloid hypothesis of Alzheimer's disease: progress and problems on the road to therapeutics. Science. 2002; 297(5580):353–6. https://doi.org/10.1126/science.1072994 PMID: 12130773

11. Selkoe DJ, Hardy J. The amyloid hypothesis of Alzheimer's disease at 25 years. EMBO Mol Med. 2016; 8(6):595–608. https://doi.org/10.15252/emmm.201606210 PMID: 27025652

12. Selkoe DJ. The molecular pathology of Alzheimer's disease. Neuron. 1991; 6(4):487–98. https://doi.org/10.1016/0896-6273(91)90052-2 PMID: 1673054

13. Paula-Lima AC, Adasme T, SanMartin C, Sebollela A, Hetz C, Carrasco MA, et al. Amyloid $\beta$-peptide oligomers stimulate RyR-mediated Ca$^{2+}$ release inducing mitochondrial fragmentation in hippocampal neurons and prevent RyR-mediated dendritic spine remodeling produced by BDNF. Antioxid Redox Signal. 2011; 14(7):1209–23. https://doi.org/10.1089/ars.2010.3287 PMID: 20712397

14. Shtifman A, Ward CW, Laver DR, Bannister ML, Lopez JR, Kitazawa M, et al. Amyloid-$\beta$ protein impairs Ca$^{2+}$ release and contractility in skeletal muscle. Neurobiol Aging. 2010; 31(12):2080–90. https://doi.org/10.1016/j.neurobiolaging.2008.11.003 PMID: 19108934

15. Demuro A, Smith M, Parker I. Single-channel Ca$^{2+}$ imaging implicates A$\beta$1-42 amyloid pores in Alzheimer's disease pathology. J Cell Biol. 2011; 195(3):515–24. https://doi.org/10.1083/jcb.201104133 PMID: 22024165

16. Ullah G, Demuro A, Parker I, Pearson JE. Analyzing and Modeling the Kinetics of Amyloid Beta Pores Associated with Alzheimer's Disease Pathology. PLoS One. 2015; 10(9):e0137357. https://doi.org/10.1371/journal.pone.0137357 PMID: 26348728

17. Berridge MJ, Bootman MD, Roderick HL. Calcium signalling: dynamics, homeostasis and remodelling. Nat Rev Mol Cell Biol. 2003; 4(7):517–29. https://doi.org/10.1038/nrm1155 PMID: 12838335

18. Dupont G, Falcke M, Kirk V, Sneyd J. Models of Calcium Signaling. Springer International Publishing Switzerland; 2016.

19. Fall CP, Marland ES, Wagner JM, Tyson JJ. Computational Cell Biology. New York: Springer Science +Business Media, Inc.; 2002.

20. Keener J, Sneyd J. Mathematical Physiology I: Cellular Physiology. 2nd ed. Springer Science+Business Media, LLC; 2009.

21. Manninen T, Havela R, Linne ML. Computational Models for Calcium-Mediated Astrocyte Functions. Front Comput Neurosci. 2018; 12:14. https://doi.org/10.3389/fncom.2018.00014 PMID: 29670517

22. Berridge MJ. The Inositol Trisphosphate/Calcium Signaling Pathway in Health and Disease. Physiol Rev. 2016; 96(4):1261–96. https://doi.org/10.1152/physrev.00006.2016 PMID: 27512009

23. Berridge MJ. Inositol trisphosphate and calcium signalling. Nature. 1993; 361(6410):315–25. https://doi.org/10.1038/361315a0 PMID: 8381210

24. Sneyd J, Dufour JF. A dynamic model of the type-2 inositol trisphosphate receptor. Proc Natl Acad Sci U S A. 2002; 99(4):2398–403. https://doi.org/10.1073/pnas.032281999 PMID: 11842185

25. Sneyd J, Tsaneva-Atanasova K, Bruce JI, Straub SV, Giovannucci DR, Yule DI. A model of calcium waves in pancreatic and parotid acinar cells. Biophys J. 2003; 85(3):1392–405. https://doi.org/10.1016/S0006-3495(03)74572-X PMID: 12944257

26. De Young GW, Keizer J. A single-pool inositol 1,4,5-trisphosphate-receptor-based model for agonist-stimulated oscillations in $Ca^{2+}$ concentration. Proceedings of the National Academy of Sciences. 1992; 89(20):9895–9899. https://doi.org/10.1073/pnas.89.20.9895

27. Othmer H, Tang Y. Oscillations and waves in a model of InsP3-controlled calcium dynamics. In: Othmer H, Murry J, Maini P, editors. Experimental and Theoretical Advances in Biological Pattern Formation. vol. 259. London: Plenum Press; 1993. p. 277–300.

28. LeBeau AP, Yule DI, Groblewski GE, Sneyd J. Agonist-dependent phosphorylation of the inositol 1,4,5-trisphosphate receptor: A possible mechanism for agonist-specific calcium oscillations in pancreatic acinar cells. J Gen Physiol. 1999; 113(6):851–72 PMID: 10352035

29. Friel DD. [Ca2+]i oscillations in sympathetic neurons: an experimental test of a theoretical model. Biophys J. 1995; 68(5):1752–66. https://doi.org/10.1016/S0006-3495(95)80352-8 PMID: 7612818

30. Dupont G, Goldbeter A. One-pool model for $Ca^{2+}$ oscillations involving $Ca^{2+}$ and inositol 1,4,5-trisphosphate as co-agonists for $Ca^{2+}$ release. Cell Calcium. 1993; 14(4):311–22. https://doi.org/10.1016/0143-4160(93)90052-8 PMID: 8370067

31. Lytton J, Westlin M, Burk SE, Shull GE, MacLennan DH. Functional comparisons between isoforms of the sarcoplasmic or endoplasmic reticulum family of calcium pumps. J Biol Chem. 1992; 267 (20):14483–9. PMID: 1385815

32. Favre CJ, Schrenzel J, Jacquet J, Lew DP, Krause KH. Highly supralinear feedback inhibition of $Ca^{2+}$ uptake by the $Ca^{2+}$ load of intracellular stores. J Biol Chem. 1996; 271(25):14925–30. https://doi.org/10.1074/jbc.271.25.14925 PMID: 8662967

33. Mogami H, Tepikin AV, Petersen OH. Termination of cytosolic $Ca^{2+}$ signals: $Ca^{2+}$ reuptake into intracellular stores is regulated by the free $Ca^{2+}$ concentration in the store lumen. EMBO J. 1998; 17(2):435–42. https://doi.org/10.1093/emboj/17.2.435 PMID: 9430635

34. Hodgkin AL, Huxley AF. A quantitative description of membrane current and its application to conduction and excitation in nerve. J Physiol. 1952; 117(4):500–44. https://doi.org/10.1113/jphysiol.1952.sp004764 PMID: 12991237

35. Seifert G, Henneberger C, Steinhäuser C. Diversity of astrocyte potassium channels: An update. Brain Res Bull. 2018; 136:26–36. https://doi.org/10.1016/j.brainresbull.2016.12.002 PMID: 27965079

36. Breslin K, Wade JJ, Wong-Lin K, Harkin J, Flanagan B, Van Zalinge H, et al. Potassium and sodium microdomains in thin astroglial processes: A computational model study. PLoS Comput Biol. 2018; 14(5):e1006151. https://doi.org/10.1371/journal.pcbi.1006151 PMID: 29775457

37. Dallérac G, Chever O, Rouach N. How do astrocytes shape synaptic transmission? Insights from electrophysiology. Front Cell Neurosci. 2013; 7:159. https://doi.org/10.3389/fncel.2013.00159 PMID: 24101894

**38.** Sibille J, Dao Duc K, Holcman D, Rouach N. The neuroglial potassium cycle during neurotransmission: role of Kir4.1 channels. PLoS Comput Biol. 2015; 11(3):e1004137. https://doi.org/10.1371/journal.pcbi.1004137 PMID: 25826753

**39.** LeBeau AP, Van Goor F, Stojilkovic SS, Sherman A. Modeling of membrane excitability in gonadotro-pin-releasing hormone-secreting hypothalamic neurons regulated by Ca2+-mobilizing and adenylyl cyclase-coupled receptors. J Neurosci. 2000; 20(24):9290–7. https://doi.org/10.1523/JNEUROSCI.20-24-09290.2000 PMID: 11125008

**40.** Demuro A, Parker I, Stutzmann GE. Calcium signaling and amyloid toxicity in Alzheimer disease. J Biol Chem. 2010; 285(17):12463–8. https://doi.org/10.1074/jbc.R109.080895 PMID: 20212036

**41.** Itkin A, Dupres V, Dufrêne YF, Bechinger B, Ruysschaert JM, Raussens V. Calcium ions promote for-mation of amyloid $\beta$-peptide (1-40) oligomers causally implicated in neuronal toxicity of Alzheimer's dis-ease. PLoS One. 2011; 6(3):e18250. https://doi.org/10.1371/journal.pone.0018250 PMID: 21464905

**42.** De Caluwé J, Dupont G. The progression towards Alzheimer's disease described as a bistable switch arising from the positive loop between amyloids and Ca(2+). J Theor Biol. 2013; 331:12–8. https://doi.org/10.1016/j.jtbi.2013.04.015 PMID: 23614875

**43.** Briggs CA, Chakroborty S, Stutzmann GE. Emerging pathways driving early synaptic pathology in Alz-heimer's disease. Biochem Biophys Res Commun. 2017; 483(4):988–997. https://doi.org/10.1016/j.bbrc.2016.09.088 PMID: 27659710

**44.** Del Prete D, Checler F, Chami M. Ryanodine receptors: physiological function and deregulation in Alz-heimer disease. Mol Neurodegener. 2014; 9:21. https://doi.org/10.1186/1750-1326-9-21 PMID: 24902695

**45.** Liang J, Kulasiri D, Samarasinghe S. Ca$^{2+}$ dysregulation in the endoplasmic reticulum related to Alzhei-mer's disease: A review on experimental progress and computational modeling. Biosystems. 2015; 134:1–15. https://doi.org/10.1016/j.biosystems.2015.05.003 PMID: 25998697

**46.** Briggs CA, Schneider C, Richardson JC, Stutzmann GE. beta amyloid peptide plaques fail to alter evoked neuronal calcium signals in APP/PS1 Alzheimer's disease mice. Neurobiol Aging. 2013; 34 (6):1632–43. https://doi.org/10.1016/j.neurobiolaging.2012.12.013 PMID: 23337342

**47.** Chakroborty S, Stutzmann GE. Calcium channelopathies and Alzheimer's disease: Insight into thera-peutic success and failures. Eur J Pharmacol. 2014; 739:83–95. https://doi.org/10.1016/j.ejphar.2013.11.012 PMID: 24316360

**48.** Goussakov I, Miller MB, Stutzmann GE. NMDA-mediated Ca(2+) influx drives aberrant ryanodine receptor activation in dendrites of young Alzheimer's disease mice. J Neurosci. 2010; 30(36):12128–37. https://doi.org/10.1523/JNEUROSCI.2474-10.2010 PMID: 20826675

**49.** Stutzmann GE, Smith I, Caccamo A, Oddo S, Laferla FM, Parker I. Enhanced ryanodine receptor recruitment contributes to Ca$^{2+}$ disruptions in young, adult, and aged Alzheimer's disease mice. J Neu-rosci. 2006; 26(19):5180–9. https://doi.org/10.1523/JNEUROSCI.0739-06.2006 PMID: 16687509

**50.** Costa RO, Lacor PN, Ferreira IL, Resende R, Auberson YP, Klein WL, et al. Endoplasmic reticulum stress occurs downstream of GluN2B subunit of N-methyl-d-aspartate receptor in mature hippocampal cultures treated with amyloid-beta oligomers. Aging Cell. 2012; 11(5):823–33. https://doi.org/10.1111/j.1474-9726.2012.00848.x PMID: 22708890

**51.** Ferreira IL, Bajouco LM, Mota SI, Auberson YP, Oliveira CR, Rego AC. Amyloid beta peptide 1-42 dis-turbs intracellular calcium homeostasis through activation of GluN2B-containing N-methyl-d-aspartate receptors in cortical cultures. Cell Calcium. 2012; 51(2):95–106. https://doi.org/10.1016/j.ceca.2011.11.008 PMID: 22177709

**52.** MATLAB 2017b, The MathWorks, Inc., Natick, MA, USA; 2017.

**53.** Doedel EJ. AUTO: A program for the automatic bifurcation and analysis of autonomous systems. In: Proc. 10th Manitoba Conf. Num. Anal. and Comp.; 1981. p. 265–284.

**54.** Ermentrout B. Simulating, Analyzing, and Animating Dynamical Systems: A Guide to XPPAUT for Researchers and Students. Philadelphia: SIAM; 2002.

**55.** Brøns M, Desroches M, Krupa M. Mixed-Mode Oscillations Due to a Singular Hopf Bifurcation in a For-est Pest Model. Mathematical Population Studies. 2015; 22(2):71–79. https://doi.org/10.1080/08898480.2014.925344

**56.** Desroches M, Guckenheimer J, Krauskopf B, Kuehn C, Osinga HM, Wechselberger M. Mixed-Mode Oscillations with Multiple Time Scales. SIAM Review. 2012; 54(2):211–288. https://doi.org/10.1137/100791233

**57.** Harvey E, Kirk V, Wechselberger M, Sneyd J. Multiple Timescales, Mixed Mode Oscillations and Canards in Models of Intracellular Calcium Dynamics. Journal of Nonlinear Science. 2011; 21(5):639–683. https://doi.org/10.1007/s00332-011-9096-z

58. Sims CE, Allbritton NL. Metabolism of inositol 1,4,5-trisphosphate and inositol 1,3,4,5-tetrakisphosphate by the oocytes of Xenopus laevis. J Biol Chem. 1998; 273(7):4052–8. https://doi.org/10.1074/jbc.273.7.4052 PMID: 9461597

59. Politi A, Gaspers LD, Thomas AP, Hofer T. Models of IP$_3$ and Ca$^{2+}$ oscillations: frequency encoding and identification of underlying feedbacks. Biophys J. 2006; 90(9):3120–33. https://doi.org/10.1529/biophysj.105.072249 PMID: 16500959

60. Supnet C, Bezprozvanny I. The dysregulation of intracellular calcium in Alzheimer disease. Cell Calcium. 2010; 47(2):183–9. https://doi.org/10.1016/j.ceca.2009.12.014 PMID: 20080301

61. Abramov AY, Canevari L, Duchen MR. Changes in intracellular calcium and glutathione in astrocytes as the primary mechanism of amyloid neurotoxicity. J Neurosci. 2003; 23(12):5088–95. https://doi.org/10.1523/JNEUROSCI.23-12-05088.2003 PMID: 12832532

62. Abramov AY, Canevari L, Duchen MR. Calcium signals induced by amyloid beta peptide and their consequences in neurons and astrocytes in culture. Biochim Biophys Acta. 2004; 1742(1-3):81–7. https://doi.org/10.1016/j.bbamcr.2004.09.006 PMID: 15590058

63. Pannasch U, Vargová L, Reingruber J, Ezan P, Holcman D, Giaume C, et al. Astroglial networks scale synaptic activity and plasticity. Proc Natl Acad Sci U S A. 2011; 108(20):8467–72. https://doi.org/10.1073/pnas.1016650108 PMID: 21536893

64. Kenny A, Plank MJ, David T. The role of astrocytic calcium and TRPV4 channels in neurovascular coupling. J Comput Neurosci. 2018; 44(1):97–114. https://doi.org/10.1007/s10827-017-0671-7 PMID: 29152668

65. Tang J, Liu T, Luo J, Yang X. Effect of calcium channel noise in astrocytes on neuronal transmission. Communications in Nonlinear Science and Numerical Simulation. 2016; 32:262–272. https://doi.org/10.1016/j.cnsns.2015.08.019

66. Ries M, Sastre M. Mechanisms of A$\beta$ Clearance and Degradation by Glial Cells. Frontiers in Aging Neuroscience. 2016; 8(160). https://doi.org/10.3389/fnagi.2016.00160 PMID: 27458370

67. Palop JJ, Mucke L. Amyloid-beta-induced neuronal dysfunction in Alzheimer's disease: from synapses toward neural networks. Nat Neurosci. 2010; 13(7):812–8. https://doi.org/10.1038/nn.2583 PMID: 20581818

68. Ripoli C, Cocco S, Li Puma DD, Piacentini R, Mastrodonato A, Scala F, et al. Intracellular accumulation of amyloid-$\beta$ (A$\beta$) protein plays a major role in A$\beta$-induced alterations of glutamatergic synaptic transmission and plasticity. J Neurosci. 2014; 34(38):12893–903. https://doi.org/10.1523/JNEUROSCI.1201-14.2014 PMID: 25232124

69. Ripoli C, Piacentini R, Riccardi E, Leone L, Li Puma DD, Bitan G, et al. Effects of different amyloid $\beta$-protein analogues on synaptic function. Neurobiol Aging. 2013; 34(4):1032–44. https://doi.org/10.1016/j.neurobiolaging.2012.06.027 PMID: 23046860

70. Selkoe DJ. Alzheimer's disease is a synaptic failure. Science. 2002; 298(5594):789–91. https://doi.org/10.1126/science.1074069 PMID: 12399581

71. Dehkordy SR, Bahrami F, Janahmadi M. Computational study of the role of calcium in late long-term potentiation induction on the basis of tripartite synapse structure. In: Proceeding from (ICEE) Electrical Engineering 22nd Iranian Conference; 2014.

72. Popugaeva E, Bezprozvanny I. Role of endoplasmic reticulum Ca$^{2+}$ signaling in the pathogenesis of Alzheimer disease. Front Mol Neurosci. 2013; 6:29. https://doi.org/10.3389/fnmol.2013.00029 PMID: 24065882

73. Li YX, Rinzel J. Equations for InsP3 receptor-mediated [Ca2+]$_i$ oscillations derived from a detailed kinetic model: a Hodgkin-Huxley like formalism. J Theor Biol. 1994; 166(4):461–73. https://doi.org/10.1006/jtbi.1994.1041 PMID: 8176949

74. Keizer J, Levine L. Ryanodine receptor adaptation and Ca$^{2+}$(-)induced Ca$^{2+}$ release-dependent Ca$^{2+}$ oscillations. Biophys J. 1996; 71(6):3477–87. https://doi.org/10.1016/S0006-3495(96)79543-7 PMID: 8968617